

1                   **Very-long-period seismicity over the 2008-2018**  
2                   **eruption of Kīlauea Volcano**

3                   **Josh Crozier<sup>1</sup>, Leif Karlstrom<sup>1</sup>**

4                   <sup>1</sup>Department of Earth Sciences, University of Oregon, Eugene, Oregon, USA.

5                   **Key Points:**

- 6                   • Developed workflow for cataloging VLP volcano seismicity with wavelet transforms  
7                   • Timeline of 2008-2018 Kīlauea Volcano magma resonance shows variability over  
8                   hours to years  
9                   • Identified variable correlations between VLP seismicity, ground deformation, and  
10                  lava-lake elevation at Kīlauea Volcano

---

Corresponding author: Josh Crozier, [jcrozier@uoregon.edu](mailto:jcrozier@uoregon.edu)

**Abstract**

Very-long-period (VLP) volcano seismicity often represents subsurface magma movement, and thus provides insight into magma system geometry and magma properties. We develop a fully automated signal processing workflow using wavelet transforms to detect and assess period, decay rate, and ground motions of resonant VLP signals. We then generate and analyze a catalog of VLP seismicity over the 2008-2018 open-vent summit eruptive episode at Kilauea Volcano, Hawaii USA. VLP seismicity occurred throughout this eruption that involved a persistent lava-lake, multiple intrusions and rift zone eruptions, and a climactic caldera collapse. We characterize trends in two dominant magma resonances: the fundamental eigenmode of the shallow magma system is a vertical oscillation of the magma column in the conduit and lava-lake, and higher frequency eigenmodes largely consist of lateral lava-lake sloshing. VLP seismicity was mainly triggered by lava-lake surface perturbations, and less commonly from depth. Variation in periods and quality factors occurred on timescales from hours to years. VLP seismicity exhibited varying correlations over time with other datasets such as ground tilt, SO<sub>2</sub> emissions, and lava-lake elevation. Variation in VLP properties also occurred over days to months preceding and following intrusions and rift zone eruptions. Changes in VLP ground motions over various timescales indicate evolution of shallow magma system geometry, which contributed to the variation in resonance. However much of the variation on timescales less than months is likely from changing magma density and viscosity, reflecting a variable shallow magmatic outgassing and convective regime within the open conduit over the ten year eruption.

**1 Introduction**

Volcano seismicity provides vital information for studying processes inside volcanoes and for monitoring changes in volcanic activity that inform hazards (e.g., Chouet & Matoza, 2013; Ripepe et al., 2015; McNutt & Roman, 2015). Amongst the rich variety of seismic signals that are commonly observed at volcanoes, so-called very-long-period (VLP) seismic events are of particular interest for magmatism as they likely represent fluid movement and/or resonance in magmatic transport structures (e.g., Chouet & Matoza, 2013; Jolly et al., 2017; Cesca et al., 2020). This type of seismicity can provide otherwise unobtainable in situ insight into magma properties and magma plumbing system geometry, and can be sensitive to different properties of the system than the longer timescale deformation observed with geodesy (e.g., Kumagai, 2006; Chouet et al., 2008; Dawson et al., 2011).

VLP seismicity is typically defined as having a disproportionate amount of energy at periods greater than  $\sim 2$  s (Chouet & Matoza, 2013). VLP seismicity can occur as isolated impulses, oscillations persisting for multiple cycles (often exhibiting roughly exponential decay over time), or tremor that can persist for hours-days or longer; and waveforms can be either periodic (with energy focused into discrete spectral peaks including harmonics), exhibit ‘gliding’ frequencies that change smoothly over time, or irregular (e.g., Aster et al., 2008; Arciniega-Ceballos et al., 2008; Haney et al., 2013; Chouet & Matoza, 2013). VLP seismicity at volcanoes has been proposed to represent various processes including magma transport through constrictions, bubble slug ascent, pressure changes in hydrothermal systems, or resonant oscillations of magma flowing within plumbing system components (e.g., Kumagai et al., 2003; Aster, 2003; Lokmer et al., 2008; Nakamichi et al., 2009; Chouet & Matoza, 2013; Dawson & Chouet, 2014; Cesca et al., 2020). Signals in volcanic settings that have been proposed to represent resonance of either magma or hydrothermal fluids often also occur in the so-called long-period (LP) band (typically 0.2-2 s) (e.g., Chouet & Matoza, 2013; Chouet & Dawson, 2016), and some can also be detected in infrasound data (e.g., Garcés et al., 2009; Fee & Matoza, 2013; Matoza et al., 2018). Isolated VLP events have been documented to be triggered by a variety of processes including eruptions, gas slug release, rapid depressurization of magmatic or hy-

drothermal features, rockfalls into a lava-lake, or tectonic events (e.g., Lyons & Waite, 2011; Maeda & Takeo, 2011; Orr et al., 2013; Chouet & Matoza, 2013). Persistent forcing could be caused by repeating discrete triggers or processes such as magma flow through irregular channels, bubble-cloud oscillations, or turbulence (e.g., Julian, 1994; Hellweg, 2000; Matoza et al., 2010; Unglert & Jellinek, 2015).

Here we develop an automated signal processing workflow for cataloging VLP seismic events from continuous seismic data, then apply this workflow to generate and analyze a catalog of VLP seismicity at Kilauea Volcano from 2008-2018. We focus on classifying signals that consist of periodic oscillations with impulsive onsets and monotonic decays in amplitude over time, as are produced by damped magma resonance. Our methods yield more robust and precise estimates of quality factors than previous approaches and are readily applicable to near-real-time monitoring and/or to other volcanic settings. Our catalog reveals the rich dynamics of Kilauea VLP seismicity, which we contextualized by comparing to other geophysical data and observed volcanic activity. We argue that this catalog informs the evolution of the Kilauea shallow magma system over 10 years, representing a unique window into the dynamics of a long-lived open-system eruption.

### 1.1 Cataloging VLP seismicity

Numerous studies have created catalogs of long-period and very-long period volcanic seismicity (e.g., Battaglia, 2003; Aster et al., 2008; Dawson et al., 2010; Zuccarello et al., 2013; Dawson & Chouet, 2014; Knox et al., 2018; Wech et al., 2020; Park et al., 2020). These signals can require different detection approaches than tectonic earthquakes, and all the previously used approaches have some limitations that motivate development of a new workflow for cataloging the resonant signals of interest here.

Time-domain moving short-term-average/long-term-average (STA/LTA) detectors will miss many events with small signal/noise ratios (Schaff, 2008). Correlation-based template matching can be much more sensitive (Schaff, 2008) and has been used to detect long-period seismicity (e.g., Aster et al., 2008; Wech et al., 2020; Park et al., 2020), but is better suited to detecting repeating events than signals that exhibit a continuum of variation (i.e., in periods, decay rates, and trigger mechanisms) and is computationally slow (Yoon et al., 2015). Approaches using feature-extraction to create and cluster waveform ‘fingerprints’ thus far are also best suited to detecting repeating events (Yoon et al., 2015). Supervised machine learning approaches can be effective for detecting earthquakes (e.g., Perol et al., 2018; Jennings et al., 2019; Bergen & Beroza, 2019) and very-long-period seismicity (Dawson et al., 2010), but can require lots of pre-selected training examples, may not detect new types of signals robustly, will generally need at least partial re-design and/or re-training to be applied to new networks/volcanoes, and their ‘black box’ nature can make predicting when or why they fail difficult (e.g., Bell, 2014; Goodfellow et al., 2016). Unsupervised learning methods have been used to cluster seismic data (Kohler et al., 2010; Mousavi et al., 2019), but have not yet been demonstrated to generate accurate or comprehensive event catalogs.

Accurately categorizing resonant VLP signals is also important, since the dominant periods, decay rates (quantified by quality factor  $Q$ , a ratio of energy stored to energy lost per cycle), and source motions (from ground motion patterns) can encode the underlying mechanism (e.g., Kumagai & Chouet, 2000; Kumagai et al., 2010). Several methods have previously been used to estimate  $Q$ . The simplest is to calculate the full width at half the maximum amplitude (FWHM) of peaks in the power spectrum. This technique is often inaccurate in the presence of noise, complicated signal shapes, or multiple signals with similar frequency components (e.g., Kumazawa et al., 1990; Zadler et al., 2004). To overcome this limitation, autoregressive (AR) methods that fit decaying sinusoids to the coda of signals were developed (Kumazawa et al., 1990; Nakano et al., 1998; Lesage et al., 2002). When the coda of a signal can be appropriately isolated these

114 methods work well for classifying dominant resonant oscillations. However, they often  
 115 do not accurately detect or estimate  $Q$  of secondary oscillations or oscillations with coda  
 116 interrupted by other signals (Fig. S1). Bandpass filtering can help isolate signals, but  
 117 often a narrow passband is required which artificially increases  $Q$  (Kumazawa et al., 1990).

118 We use continuous wavelet transforms (CWTs) to detect and classify  $T$ ,  $Q$ , and ground  
 119 motion patterns of resonant VLP seismic signals. CWTs are a method for determining  
 120 the frequency content of signals over time (e.g., Alsberg et al., 1997; Selesnick et al., 2005)  
 121 that have been previously used to analyze volcano seismicity and suggested as a means  
 122 for automated signal detection and classification (Lesage, 2009; Lapins et al., 2020). Our  
 123 methods can robustly determine  $T$  and  $Q$  in the presence of high noise, multiple reso-  
 124 nant frequencies, and overlapping signals. These methods are also readily extendable to  
 125 characterizing resonant signals in the LP band and in infrasound data, as well as some  
 126 periodic tremor and gliding-frequency signals, but are likely not the optimal approach  
 127 for analyzing signals that are not periodic. Our approach does not depend upon train-  
 128 ing data or templates, and thus can be applied to any instrument network or volcano  
 129 with minimal configuration.

## 130 1.2 The 2008-2018 eruption of Kīlauea Volcano

131 We examine the 2008-2018 summit eruptive episode of Kīlauea Volcano, a basaltic  
 132 shield volcano on the island of Hawaii. This was the most recent period of continuous  
 133 summit activity following decades of quiescence or sporadic events largely focused along  
 134 the East Rift Zone (ERZ) (e.g., Wright & Klein, 2014). Over this timespan a summit  
 135 lava-lake persisted at the surface, then drained as part of a caldera collapse eruption se-  
 136 quence in May-August 2018 (e.g., Neal et al., 2019; Patrick, Orr, et al., 2019; Patrick,  
 137 Swanson, & Orr, 2019). Kīlauea is one of the best monitored volcanoes in the world, with  
 138 abundant data on ground deformation (from tilt-meters, GPS/GNSS stations, and In-  
 139 SAR), gas flux, magma composition, and lava-lake activity (e.g., Edmonds et al., 2015;  
 140 Elias et al., 2018; Patrick, Swanson, & Orr, 2019) that can contextualize VLP seismic-  
 141 ity.

142 The U.S. Geological Survey Hawaii Volcano Observatory operates a dense broad-  
 143 band seismic network at Kīlauea Volcano. VLP seismicity at Kīlauea has previously been  
 144 cataloged up to 2013 using a hidden Markov model to detect events and the Sompi AR  
 145 method to determine  $T$  and  $Q$  of these events (Dawson et al., 2010; Dawson & Chouet,  
 146 2014); this existing catalog provides an important benchmark for our methods. We find  
 147 prevalent VLP seismicity over the 2008-2018 timespan, representing a rich probe of changes  
 148 within the shallow subsurface magma system of Kīlauea Volcano on a variety of timescales.

## 149 2 Methods

### 150 2.1 Seismic data

151 The first step in our workflow is selecting and processing seismic data (Fig. 1). We  
 152 use waveforms from 3-component broadband seismometers in the Hawaii Volcano Ob-  
 153 servatory (HVO) network (USGS, 1956) that are within  $\sim 3$  km of the vent. We use avail-  
 154 able data from the following stations: NPB, NPT, SRM, OBL, WRM, SDH, UWE, UWB,  
 155 SBL, KKO, and RIMD (Fig. 2, 3). Some other stations in the area were not used due  
 156 to low signal/noise ratios. Seismic data from 2008-2011 was obtained from the USGS,  
 157 subsequent data is publicly available from IRIS (Incorporated Research Institutions for  
 158 Seismology). We download and process data in 6 hr time windows and discard waveforms  
 159 with data gaps longer than 2 s.

160 We deconvolve the instrument responses to facilitate stacking of data from differ-  
 161 ent instruments (Fig. S2). A standard ‘water level’ is first applied to these instrument

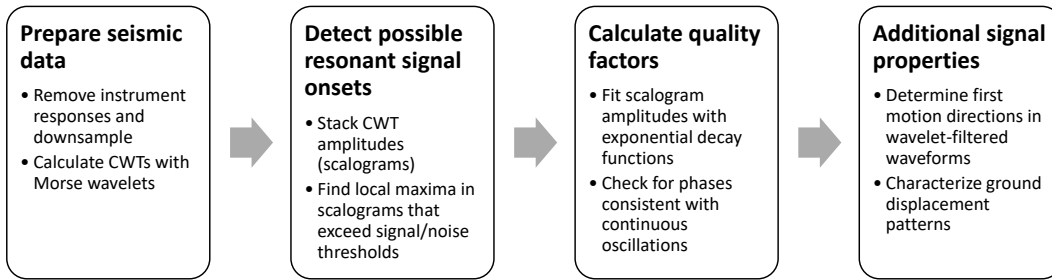


**Figure 1.** Signal processing workflow for VLP detection and characterization.

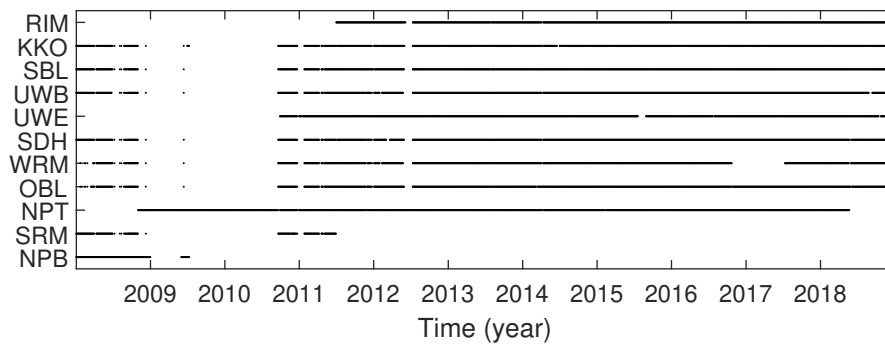


**Figure 2.** Timeline of data availability at the HVO broadband seismic stations used in this study.

162 responses so that the maximum amplification is 10 times the base amplification. This  
 163 prevents over-magnification of noise at periods outside of the instrument sensitivity range.  
 164 We note that this process is not causal and can introduce artificial tapers around dis-  
 165 continuities (e.g., step functions); an effect included in the synthetic seismograms we use  
 166 to test our methods (Appendix A). All waveforms are then smoothed and resampled at  
 167 6 Hz (much higher than the signal frequencies of interest).

## 168 2.2 Continuous wavelet transforms

169 The second step (Fig. 1) in our method involves calculating time-frequency rep-  
 170 resentations of the seismic data, which are well suited to identifying resonant signals (e.g.,  
 171 Köcher et al., 2014). We use continuous wavelet transforms (CWTs), which offer sev-  
 172 eral advantages over standard short-time Fourier-transforms (STFTs). CWTs involve  
 173 specifying a base wavelet that can be stretched or ‘scaled’ to different frequencies and  
 174 cross-correlated with data to determine frequency content as a function of time (e.g., Als-  
 175 berg et al., 1997; Selesnick et al., 2005). Plots of CWT amplitudes are termed scalograms.  
 176 For a given wavelet CWTs provide increasing temporal resolution with increasing fre-  
 177 quency; this is a primary advantage over STFTs which have the same temporal resolu-  
 178 tion for all frequencies (e.g., Lapins et al., 2020).

179 Useful wavelets for time-frequency analysis are often sinusoids scaled by some func-  
 180 tion with symmetric, compact support that decays in both directions from a central point

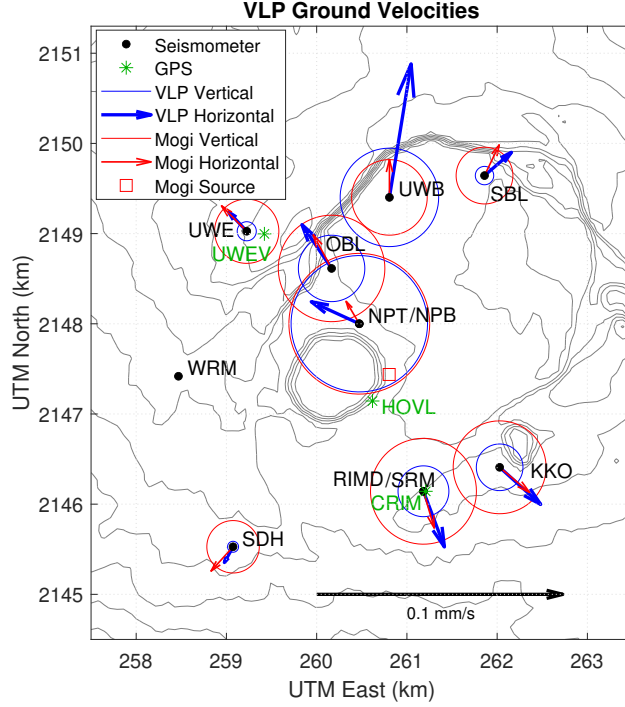


**Figure 3.** Map of seismometers and GPS stations also showing ground velocities and Mogi inflating spherical reservoir source inversions results for an example conduit-reservoir event on 2017-5-21 (plotted at the time of peak vertical velocity at station NPT). Horizontal velocities (arrows) and vertical velocities (circles, all positive/upward) are shown at the same scale. Horizontal components in the data and source inversion include both tilt and translation effects. UTM zone 5Q.

181 (Fig. 4). We use Morse wavelets which are given in the spectral domain (for angular fre-  
 182 quency  $\omega$ ) by:

$$\Psi_{\beta,y}(\omega) = U(\omega)a_{\beta,y}\omega^{\beta}e^{-\omega^{\gamma}} \quad (1)$$

183 where  $U(\omega)$  is the Heaviside step function,  $\beta$  governs wavelet duration (or decay rate),  
 184  $\gamma$  governs wavelet symmetry, and  $a_{\beta,y}$  is a normalizing constant (Lilly & Olhede, 2009).  
 185 We set  $\gamma = 3$  which yields wavelets that are symmetric in the frequency domain (Lilly  
 186 & Olhede, 2009).

187 Increasing wavelet duration (i.e., decreasing decay rate) will provide better frequency  
 188 resolution but worse temporal resolution (Fig. 4), analogous to increasing window length  
 189 in a STFT. An arbitrary number of ‘stretches’ of a wavelet can be used to sample at any  
 190 desired frequencies, though there is a limit to the effective frequency resolution possi-  
 191 ble with a given wavelet (Fig. 4). The gradual onset of wavelets introduces less artifi-  
 192 cial temporal ‘jaggedness’ than a standard STFT (where sinusoids truncate abruptly at  
 193 the edges of each window) which allows for more accurate determination of signal de-  
 194 cay rates. The convolution between a wavelet and an impulsive signal (such as a single  
 195 peak or step function) will have a duration and decay rate similar to the wavelet itself  
 196 (Fig. S3). This is analogous to temporal smearing of impulsive signals in STFTs over  
 197 the window length used. Thus, wavelet duration determines the minimum signal dura-  
 198 tion that can be distinguished from an impulsive signal, so narrower wavelets can resolve  
 199 lower  $Q$  oscillations.

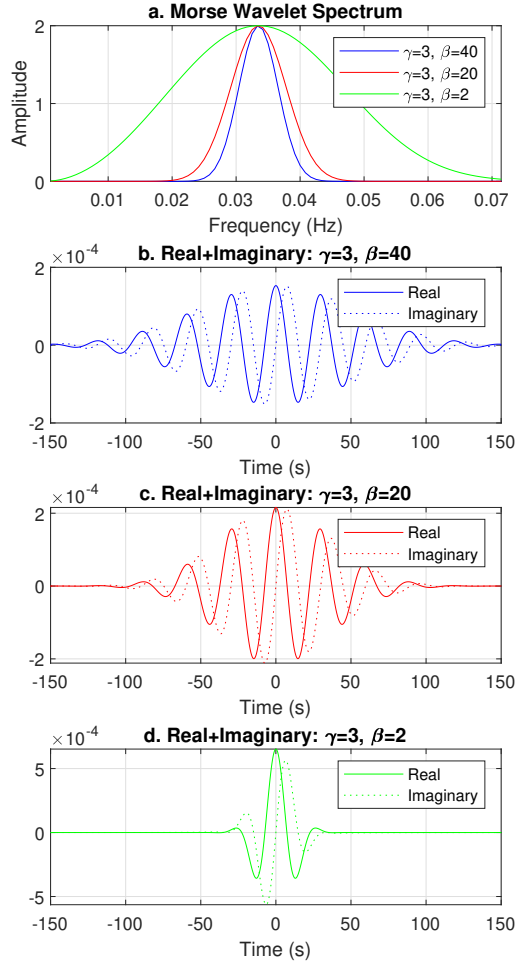


**Figure 4.** Morse wavelets used in this study (in this case scaled to a period of 30 s). (a) Amplitude spectra. (b)  $\beta = 40$  wavelet used to make combined scalograms from which potential VLP signals are detected. (c)  $\beta = 20$  wavelet used to make combined scalograms from which potential VLP signals are detected and for calculating  $Q$  of signals. (d)  $\beta = 2$  wavelet used for detecting first motions of signals.

200

### 2.3 Detecting potential resonant signal onsets

201

202

203

204

205

206

207

208

209

To mitigate the inherent trade-off between spectral and temporal resolution we make combined scalograms using wavelets with two different values of  $\beta$ , 40 and 20 (Fig. 4). The higher frequency resolution of the  $\beta = 40$  wavelet helps more accurately determine resonant signal period. The  $\beta = 20$  wavelet still provides enough frequency resolution to isolate typical Kilauea VLP signals (Fig. S4), but its increased temporal resolution helps reveal gaps that could indicate whether a signal is a continuous oscillation (Fig. S5) and helps resolve signals with lower  $Q$  (Fig. S3). We exclude periods less than 10 s in this study because of the strong oceanic microseism at these periods over the Kilauea seismic network (e.g., Berger et al., 2004; Dawson & Chouet, 2014). We stack the scalo-

210 grams from all available stations to increase the signal/noise ratio. Given the proxim-  
 211 ity of our stations, travel time effects from seismic waves are negligible at periods of in-  
 212 terest. For shear wave speeds of 1800 m/s (e.g., Dawson et al., 1999; Lin et al., 2014),  
 213 the wavelength of a 10 s period wave will be 18 km, roughly four times the distance across  
 214 our  $\sim 5$  km wide array. There is also no concern about destructive interference from stack-  
 215 ing scalograms since they contain no phase information. For applying our workflow to  
 216 shorter period resonant signals (e.g., some LP events), more expansive instrument ar-  
 217 rays, or infrasound data travel time effects may need to be considered.

218 To detect potential resonant signal onsets in a stacked scalogram, we first calcu-  
 219 late moving long-term averages (LTA) and moving standard deviations of each frequency  
 220 component with 200 s windows (Fig. 5). We then introduce a frequency-dependent de-  
 221 lay of four cycles to the LTA and standard deviation to account for non-causality in the  
 222 scalogram. Next, in each frequency band of the stacked scalogram we identify all points  
 223 that are local maxima, have amplitudes that are above some chosen multiple of the LTA  
 224 (which we term the STA/LTA threshold), and are also more than some threshold num-  
 225 ber of standard deviations above the LTA (Fig. 5). We select a value of 3 for both thresh-  
 226 olds; chosen to minimize false detections while keeping most desired signals in both syn-  
 227 thetic tests and real data (Fig. S6, S7, S8). Finally, where local maxima are separated  
 228 by both less than a ratio of 1.07 in period (the minimum separation that can be robustly  
 229 resolved with the wavelets we use) and less than 200 s in time, we keep the maxima cor-  
 230 responding to the highest energy integrated over the following two cycles. This is more  
 231 robust than just keeping the highest maxima.

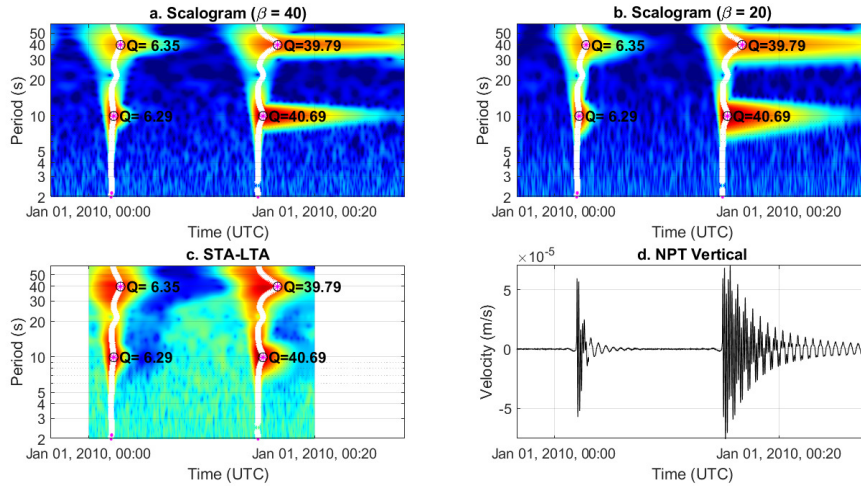


**Figure 5.** Example scalograms and cataloged events from a synthetic seismogram consisting of four VLP signals with [start time,  $T$ ,  $Q$ ] = [00:05, 40, 6], [00:05, 10, 6], [00:15, 40, 40], [00:15, 40, 40], plus white noise from a standard normal distribution scaled by 0.1% of the signal amplitude (Appendix A). Here  $T$  and  $Q$  of all resonant signals are recovered accurately. (a)  $\beta = 40$  scalogram. White dots indicate temporal local maxima that meet the minimum STA/LTA criteria, and magenta dots indicate points that are spectral local maxima (integrated over two cycles). Black circles and text indicate the final selected event onsets and corresponding calculated  $Q$ . (b)  $\beta = 20$  scalogram. (c) Frequency-dependent STA/LTA. (d) Synthetic seismogram. We note that the slight precursory oscillations arise from removing the instrument response.

232

## 2.4 Calculating quality factor ( $Q$ )

233

234

235

236

237

238

239

240

241

242

243

244

245

The third step (Fig. 1) in our workflow is calculating  $Q$  by fitting decaying exponentials to stacked scalogram amplitudes following each detected potential resonant signal onset (Fig. 6). We use only the narrower  $\beta = 20$  CWTs that have better temporal resolution (Fig. 4); the minimum  $Q$  that this wavelet can robustly resolve is around 6. Lower  $\beta$  values could be used to resolve lower  $Q$  events at the expense of worse frequency resolution. We extract scalogram amplitudes at the target frequency over one to eight cycles after the identified signal onset. The one cycle delay avoids the region near the onset of an impulsively initiated signal where amplitudes will be inherently underestimated since part of the wavelet will not be overlapping the signal (Fig. 6), and helps avoid artifacts that might be present from a trigger mechanism. Delays between 0.5 and 1.5 cycles yield negligibly different results. Eight cycles was found to be a sufficient duration for robustly capturing signal decay rates; increasing this duration further will not affect the accuracy of our fitting method.

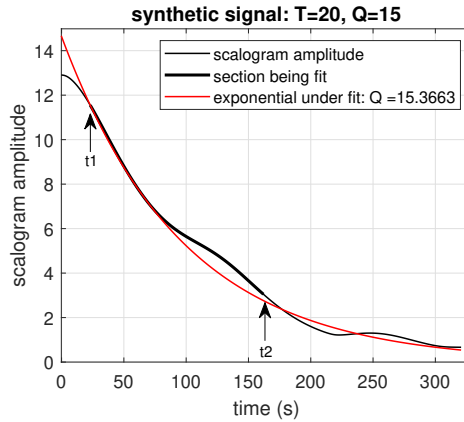


**Figure 6.** Example estimation of  $Q$  by scalogram exponential fit from a synthetic seismogram. This seismogram consists of a VLP signal with  $[T, Q] = [20 \text{ s}, 15]$ , plus white noise from a standard normal distribution scaled by 1% of the signal amplitude. The bold part of the black line shows the part of the scalogram data that is being fit (from  $t_1$  to  $t_2$ ), and the red line shows the exponential ‘under fit’ (Eq. 2).

246

247

248

249

250

251

252

253

Standard least-squares exponential regressions can underestimate decay rate in the presence of noise or where another signal starts within the fitting window, thus overestimating  $Q$  (Fig. S9). We tested a variety of different exponential fitting approaches with varying fit timespans, maxima/minima, weighting schemes, outlier exclusion methods, and goodness of fit thresholds. An ‘under-fit’ is the most robust (Fig. 6, S10), involving an exponential fit with initial amplitude fixed to the initial scalogram amplitude  $A(t_1)$  and with the slowest decay rate  $\alpha$  that remains bounded from above by scalogram amplitudes in the timespan being fit ( $t_1$  to  $t_2$ ) (Fig. 6, S9):

$$\alpha = -\min_{t=t_1}^{t_2} \left[ \frac{\ln(A(t)) - \ln(A(t_1))}{t - t_1} \right] \quad (2)$$

254

255

256

257

258

which then yields quality factor:  $Q = \pi/(T\alpha)$ . This fitting method is less sensitive to the choice of fitting timespan than least-squares regressions, since extending the timespan will have no effect unless the added amplitudes fall beneath the current fit. Additionally, other signals interrupting the coda of the target signal are less likely to affect this fitting method. The estimates from this method have a slight negative bias (<10%

259 even for very high noise levels, Fig. S10). However, this method has lower bias and higher  
 260 overall accuracy than other regression methods (Fig. S10) and outperforms the Sompi  
 261 AR method which fails to detect the signals of interest in many of our tests.

262 Signals that are not a single continuous periodic oscillation could create a contigu-  
 263 ous band of elevated energy in a scalogram that appears like a decaying resonant signal.  
 264 To mitigate this, we also extract the phases of the  $\beta = 20$  CWTs at each channel and  
 265 check for consistent trends over the timespan being fit. For a continuous periodic oscil-  
 266 lation, the phase  $\theta(t)$  of a wavelet stretched to the oscillation frequency  $f$  will increase  
 267 steadily as it is convolved with the signal (Fig. 7, S11):

$$\theta(t) = 2\pi ft + \theta(0) \quad (3)$$

268 A signal that is not a continuous periodic oscillation can exhibit deviations from this ex-  
 269 pected phase (Fig. 7). To quantify how ‘continuous’ a signal is, we calculate the mean  
 270 phase deviation ( $E_\theta$ ) from the expected phase over the timespan being fit ( $t_2 - t_1$ ) and  
 271 over all  $N$  channels:

$$E_\theta = \frac{1}{N} \frac{1}{t_2 - t_1} \sum_{n=1}^N \int_{t_1}^{t_2} |2\pi ft + \tilde{\theta}_n - \theta_n(t)| dt \quad (4)$$

272 where  $\tilde{\theta}_n$  is the constant phase offset that minimizes phase deviation at channel  $n$ . We  
 273 use this phase offset instead of the actual initial phase  $\theta_n(t_1)$  since there may be effects  
 274 from the signal onset present at the start of the timespan. We then keep only signals with  
 275 a mean phase deviation of less than a threshold value of 0.1 radians. This threshold min-  
 276 imizes inclusion of noise or non-continuous oscillations while keeping most continuous  
 277 periodic oscillations in tests on both synthetic and real data (Fig. 7, S11).

## 278 2.5 Determining first motions

279 First motions (polarities) are not well defined for signals without impulsive onsets.  
 280 Even for impulsive onsets, picking first motions for a particular frequency component  
 281 is difficult to do robustly because band-pass filtering a signal will distort the onset of that  
 282 signal regardless of the filter used (i.e., causal or acausal, FIR or IIR) (Fig. 8). To partly  
 283 mitigate this issue, we use a ‘wavelet filter’: we compute the CWT of a signal, then re-  
 284 construct the signal using an inverse CWT but keeping only the period of interest. This  
 285 still produces artificial precursory oscillations in front of signals with impulsive onsets  
 286 (Fig. 8), but the size of these oscillations is predictable for a given wavelet. We use a  
 287 very narrow Morse wavelet ( $\beta = 2$ ) which will produce only one appreciable precursory  
 288 oscillation that will be less than half of the signal amplitude, though such a narrow wavelet  
 289 will be sensitive to a wider frequency range (Fig. 4).

290 We then stack the amplitudes of the wavelet-filtered signals from all channels and  
 291 identify local maxima around the signal onset time that exceed the thresholds for both  
 292 STA/LTA and number of standard deviations above the LTA (Fig. 8). We discard lo-  
 293 cal maxima that are less than half of the global maximum, which for impulsive onset sig-  
 294 nals will exclude precursory oscillations caused by the wavelet filter. If no local maxima  
 295 remain, which will occur either if the signal has a gradual onset or is too contaminated  
 296 by other signals/noise, we consider the first motions undetermined. If one or more max-  
 297 ima remain, we select the first of these as the first motion time and then obtain corre-  
 298 sponding first motion directions at each channel from the wavelet filtered waveforms (Fig.  
 299 8). We store the STA/LTA ratio, standard deviations above the LTA, and fraction of  
 300 the global maximum for this local maximum as indicators of pick confidence.

## 301 2.6 Comparison with previous Kīlauea VLP catalog

302 We compare our catalog to one produced using the methods from Dawson and Chouet  
 303 (2014) extended through 2018: automated detection via a hidden Markov model trained

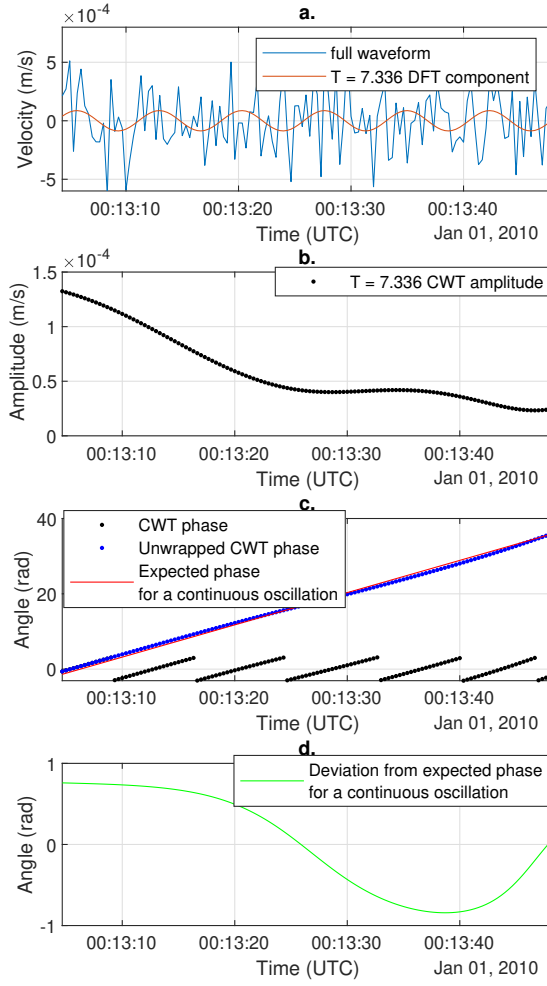


**Figure 7.** Example phase continuity from a spectral peak in synthetic random noise, where the high phase deviation correctly indicates that this is likely not a continuous oscillation. (a) Synthetic seismogram and 7.336 s DFT component. In a scalogram (or frequency spectrum) this signal exhibits a local maximum at this period. (b) CWT amplitude of the 7.336 s signal, which exhibits a roughly exponential decay. (c) CWT phase of the 7.336 s signal and expected phase for a continuous oscillation. (d) Difference between CWT phase and expected phase for a continuous oscillation.

304 on example events (Dawson et al., 2010) and estimation of  $T$  and  $Q$  via the Sompi AR  
 305 model (Kumazawa et al., 1990). For both catalogs adjustment of various threshold  
 306 parameters is required to minimize false picks and poorly constrained events. In the cat-  
 307 alog extended from Dawson and Chouet (2014) the most useful parameters to thresh-  
 308 old are event amplitude at station NPB or NPT and the standard deviation of  $Q$  from  
 309 Sompi cluster fits. We set these thresholds to 325 counts and 0.275 respectively, which  
 310 results in a similar number of events in both catalogs ( $\sim 3200$ ). In both catalogs chang-

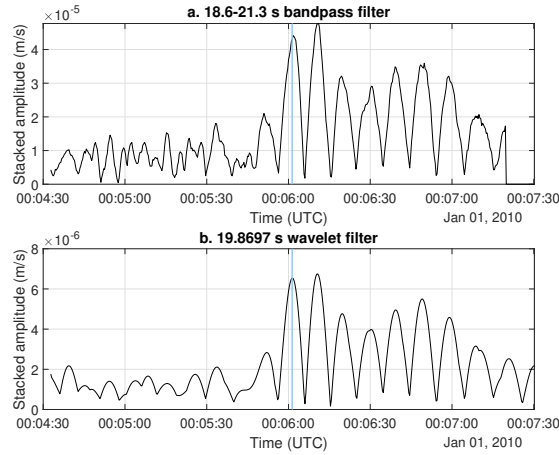


**Figure 8.** Example correct first motion pick from a synthetic seismogram for an impulsive onset oscillation with  $[\text{start time}, T, Q] = [00:06, 20, 20]$ , plus a step displacement (velocity spike) at time 00:06, plus two other equal-amplitude oscillations with  $[\text{start time}, T, Q] = [00:05, 80, 20]$  and  $[00:05, 5, 20]$ , and plus white noise from a standard normal distribution scaled by 0.1% of the signal amplitude. (a) Stacked amplitudes from waveforms filtered with an FIR bandpass filter. This is just shown for comparison and not used in picking first motions. The cyan line is the algorithm’s first motion pick. (b) Stacked amplitudes from waveforms filtered with the wavelet filter we use for picking first motions.

311 ing these thresholds will greatly vary the number of events included, and less strict thresh-  
 312 olds will include tens of thousands of additional events (Fig. S7, S8).

313 For the thresholds shown the two catalogs include around 1000 overlapping events,  
 314 most of which are part of a dominant trend of events that spans most of the timeline with  
 315 periods varying from about 15-40 s (Fig. 9). There are more total events in this main  
 316 event trend in the catalog extended from Dawson and Chouet (2014) than in ours, but  
 317 there are also many events unique to our catalog both in this main event trend and form-  
 318 ing additional event groups. Using less strict thresholds on both catalogs results in a larger  
 319 number overlapping events, primarily in the main event trend, but there are still many  
 320 events unique to each catalog. Based on visual inspections of outlier events and a ran-  
 321 dom subset of all events, at the thresholds shown both catalogs include on the order of  
 322 100 events that are likely bad detections. For this purpose we consider bad detections  
 323 either signals with estimates of  $T$  that appear inaccurate by more than  $\sim 25\%$  or signals  
 324 that do not appear to be continuous periodic oscillations (e.g., noise or tectonic earth-  
 325 quakes).

326 Accurate estimates of  $T$  and  $Q$  will be more valuable than total event counts for  
 327 inferring properties of the magmatic system. Our catalog generally includes less scatter  
 328 in both  $T$  and  $Q$  for the main event trend (most of the apparent  $Q$  outliers in Fig.  
 329 9 plot b are not from the main event trend). The lower scatter in our catalog is also present  
 330 when only comparing matching events (Fig. 9) and is present over a range of reasonable  
 331 event thresholds for both catalogs. As discussed in section 2.3, our method cannot ro-  
 332 bustly detect events with  $Q < 6$  given the wavelets we are using. The catalog extended  
 333 from Dawson and Chouet (2014) extends to lower  $Q$ , though the accuracy with which  
 334 low- $Q$  events can be characterized will be inherently limited as indicated by the large  
 335 scatter in  $T$  from late 2011-early 2012. Where the two methods estimate appreciably dif-  
 336 ferent values of  $Q$  we find that there is often some complication (such as overlapping sig-

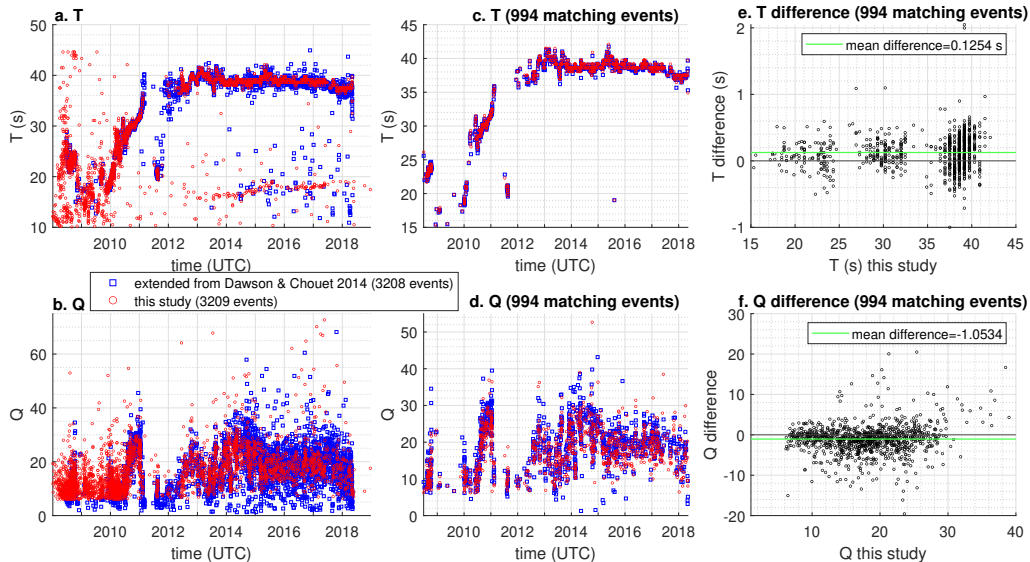


**Figure 9.** Comparison of detected VLP events from this study with a catalog extended from Dawson and Chouet (2014). Event detection thresholds were chosen to produce a similar number of events in both catalogs (section 4.1). (a and b)  $T$  and  $Q$  over time in both catalogs. (c and d)  $T$  and  $Q$  over time from corresponding events that have start times within 3 minutes of each other and  $T$  ratios within 4/5-5/4 of each other between the two catalogs. (e and f) Values of  $T$  and  $Q$  in our catalog minus values in the catalog extended from Dawson and Chouet (2014) for corresponding events.

337 nals or strong noise) that causes the Sompi AR method to be inaccurate where our method  
 338 still produces reasonable estimates.  $Q$  estimates in our catalog are very slightly lower  
 339 on average (by  $\sim 1$ ) than those of matching events in the catalog extended from Dawson  
 340 and Chouet (2014) (Fig. 9). This is consistent with the bias our exponential fitting method  
 341 exhibits for noisy synthetic signals (section 2.4, Fig. S10) which we expect is a benefi-  
 342 cial trade-off for increased precision and robustness.

343 Most prominent among the groups of events unique to our catalog is a trend of events  
 344 with  $T$  ranging from 10-20 s between 2010 and 2018 (Fig. 9). The Sompi AR method  
 345 can detect and provide accurate estimates of  $T$  for many of these events (Dawson & Chouet,  
 346 2014), but often does not produce accurate estimates of  $Q$  even with manual examina-  
 347 tion of the algorithm output. Our methods generally provide accurate estimates of  $Q$   
 348 for these events, but still exclude many real events in this band when strict enough thresh-  
 349 olds are used to minimize bad detections in the catalog as a whole. Our catalog also in-  
 350 cludes a clear event group with  $T$  around 15 s in early 2009, and some other more iso-  
 351 lated clusters between 2008 and 2010 (Fig. 9). Our catalog shows large scatter in  $T$  prior  
 352 to 2010, but many of these values do likely represent real VLP oscillations. Both cata-  
 353 logs show multiple isolated events after 2012 with  $T$  from  $\sim 10$ -15 and  $\sim 20$ -35 s. Most  
 354 of these detections in our catalog are gliding-frequency VLP events; some in the cata-  
 355 log extended from Dawson and Chouet (2014) are also gliding-frequency VLP events whereas  
 356 others do not appear to be coherent VLP oscillations.

357 In summary, both detection methods produce incomplete catalogs, particularly for  
 358 the secondary group of events with 10-20 s periods, and both involve trade-offs between  
 359 missing real events and including too many bad detections. The two catalogs contain many  
 360 non-overlapping events, so to obtain a maximally complete catalog there would be value

361 in combining both detection methods. However, since our detection method does not re-  
 362 quire labeled training data and has demonstrated performance that is comparable over-  
 363 all and better in some respects than existing approaches for detecting resonant VLP seis-  
 364 micity, we expect it will be a useful tool in various volcanic settings. Additionally, we  
 365 expect our method for estimating  $Q$  will be valuable, even if applied to events detected  
 366 via other methods, since it is demonstrably robust which should facilitate better infer-  
 367 ence of magma system properties.

## 368 2.7 Characterizing ground motion patterns

369 Our goal in this study is not to conduct detailed source inversions for every event,  
 370 but rather to quantitatively characterize when changes in ground motion patterns oc-  
 371 cur. Average phases and amplitudes at each channel are obtained using the Goertzel DFT  
 372 algorithm (Proakis & Monolakis, 1990) over a time window between one and five cycles  
 373 after each event onset. We then compute the average vertical/horizontal velocity ratio  
 374  $R_{vh}$ , defined for the target frequency component  $f$  as:

$$R_{vh} = \sum_{m=1}^M \frac{|\dot{\mathbf{u}}_{Z,m}(f)|}{|\dot{\mathbf{u}}_{E,m}(f) + \dot{\mathbf{u}}_{N,m}(f)|} \quad (5)$$

375 for vertical ( $Z$ ), east ( $E$ ), and north ( $N$ ) velocities ( $\dot{\mathbf{u}}$ ) at all  $M$  stations. This metric  
 376 requires no assumptions of source location or mechanics, but it is sensitive to tilt which  
 377 will increase the apparent amplitude of horizontal components at increasing  $T$ .

378 We also quantify how radially oriented horizontal motion vectors are by calculat-  
 379 ing the angles from the direction to an inferred source location, similar to ‘semblance’  
 380 (e.g., Legrand et al., 2000). We set this source location based on a previous geodetic (In-  
 381 SAR, GPS, and tilt) inversion for the shallow ground deflation source in early 2018 (Anderson  
 382 et al., 2019) (Fig. 3), which is similar to the centroid location inferred by other seismic  
 383 and geodetic inversions over the past decade (Chouet et al., 2010; Chouet & Dawson,  
 384 2011; Anderson et al., 2015; Anderson & Poland, 2016; Liang, Crozier, et al., 2020). We  
 385 then calculate radial misfit  $E_{radial}$  as the mean angle between the target frequency com-  
 386 ponent of observed  $\dot{\mathbf{u}}$  and predicted  $\dot{\mathbf{w}}$  (perfectly radial) velocity vectors:

$$E_{radial} = \frac{1}{MT} \sum_{m=1}^M \int_0^T \left| \arccos \left( \frac{\dot{\mathbf{u}}(t) \cdot \dot{\mathbf{w}}(t)}{|\dot{\mathbf{u}}(t)| |\dot{\mathbf{w}}(t)|} \right) \right| dt \quad (6)$$

387 The final method we use to quantify ground motion patterns is conducting source  
 388 inversions for an inflating/deflating spherical reservoir using a ‘Mogi’ model for a point  
 389 source in an elastic half-space (Mogi, 1958). The quasi-static elasticity used in the Mogi  
 390 model should be approximately valid for the long period signals and short distances con-  
 391 sidered here (see section 2.3). Due to their simplicity, these inversions are most useful  
 392 as an indicator of relative changes in source centroid depth rather than as a probe of de-  
 393 tailed reservoir geometry. For example, changes in Mogi centroid depth could represent  
 394 changes in the vertical extents of an ellipsoidal reservoir, and/or changes in the geom-  
 395 etry or activation of any secondary dikes or sills that may also be contributing to the ground  
 396 motions. Additionally, the misfit from Mogi inversions provides a second metric for the  
 397 radial symmetry of ground motions.

398 We fix the east and north Mogi source location based on previous geodetic inver-  
 399 sions to simplify the inversion results and reduce noise-induced scatter (Anderson et al.,  
 400 2019) (Fig. 3). We assume a shear modulus of 10 GPa and Poisson’s ratio of 0.25. We  
 401 include ground tilt (detected as horizontal acceleration by broadband seismometers) in  
 402 the Green’s functions (Maeda et al., 2011) to predict displacements  $\mathbf{w}$  as:

$$\mathbf{w}(f) = \left( \mathbf{G}_t + \mathbf{G}_r \frac{g}{(2\pi i f)^2} \right) P(f), \quad (7)$$

403 where  $\mathbf{G}_t$  and  $\mathbf{G}_r$  are the translation and tilt Green’s function matrices from a Mogi source  
 404 at a given depth,  $g$  is gravitational acceleration, and  $P$  is forcing pressure. We solve for  
 405 the  $P$  that results in minimal misfit between  $\mathbf{w}$  and observed displacements  $\mathbf{u}$  for given  
 406 Green’s functions using a linear least-squares inversion. We then conduct a grid search  
 407 to find the Mogi source depth that minimizes misfit  $E$  between the target frequency com-  
 408 ponent of  $\mathbf{w}$  and  $\mathbf{u}$  according to:

$$E = \frac{\sum_{n=1}^N |\mathbf{u}_n(f) - \mathbf{w}_n(f)|}{\sum_{n=1}^N |\mathbf{u}_n(f)|} \quad (8)$$

409 for all  $N$  channels, with source depth bounded between 500 m and 2500 m beneath the  
 410 caldera floor.

## 411 2.8 Other geophysical data and observations

412 To interpret the timeline of VLP seismicity cataloged in this work, we rely on a se-  
 413 ries of touchstone events that characterize the progression of the 2008-2018 Kīlauea erup-  
 414 tive episode. ERZ eruptions prior to 2018 have been compiled in Patrick, Swanson, and  
 415 Orr (2019): the March 2011 Kamoamoā fissure eruption (Orr et al., 2015), August 2011  
 416 Pu‘u ‘Ō‘ō vent opening, September 2011 Pu‘u ‘Ō‘ō vent opening, June 2014 Pu‘u ‘Ō‘ō  
 417 vent opening (Poland et al., 2016), and May 2016 Episode 61g Pu‘u ‘Ō‘ō vent opening  
 418 (Chevrel et al., 2018). Timing of the 2018 eruption is given in Neal et al. (2019). Doc-  
 419 umented summit intrusions have been compiled in Patrick, Swanson, and Orr (2019):  
 420 October 2012, May 2014, and May 2015 (Johanson et al., 2016). Regional slow-slip events  
 421 (SSEs) have been compiled in Montgomery-brown et al. (2015) and Wang et al. (2019):  
 422 February 2010, May 2012, and October 2015.

423 To indicate long-term ground deformation we use near-field (within  $\sim 2$  km of the  
 424 vent) geodetic data: vertical displacements from GPS station HOVL, horizontal line-lengths  
 425 between GPS stations UWEV and CRIM, and east and north tilt from tilt-meter UWE  
 426 (Miklius, 2008; Johanson, 2020) (Fig. 3). We also use smoothed stacks of these four datasets  
 427 to infer times of inflation and deflation. For this we smooth all four datasets with 30-  
 428 day moving average filters and scale them to have a unit range, then flip the sign of UWE  
 429 east tilt-meter data so that increasing values indicate inflation, and then stack the four  
 430 datasets. We consider any time when the stacked geodetic data is increasing to indicate  
 431 long-term inflation.

432 We use lava-lake elevation and surface area data from Patrick, Swanson, and Orr  
 433 (2019) (data extended through 2018 was obtained from the USGS HVO via Matt Patrick).  
 434 This data is obtained from a combination of webcam images, thermal images, and laser  
 435 rangefinders.  $\text{SO}_2$  gas flux data from various monitoring stations for the whole times-  
 436 pan does exist (Whitty et al., 2020), but we only consider data from published studies  
 437 using direct measurements of the summit plume. We use  $\text{SO}_2$  emission data collected  
 438 by a vehicle-based FLYSPEC UV spectrometer from 2007-2010 (Elias & Sutton, 2012).  
 439 We also use  $\text{SO}_2$  emission data collected by an array of FLYSPEC UV spectrometers from  
 440 2014-2017 (Elias et al., 2018). Both datasets have large uncertainties (Fig. 10, 11) due  
 441 to spectral fitting limitations and uncertainty in plume speed and location (Elias & Sut-  
 442 ton, 2012; Elias et al., 2018).

## 443 3 Results

### 444 3.1 Types of VLP seismicity at Kīlauea from 2008-2018

445 We will introduce the common types of VLP signals present in the catalog.

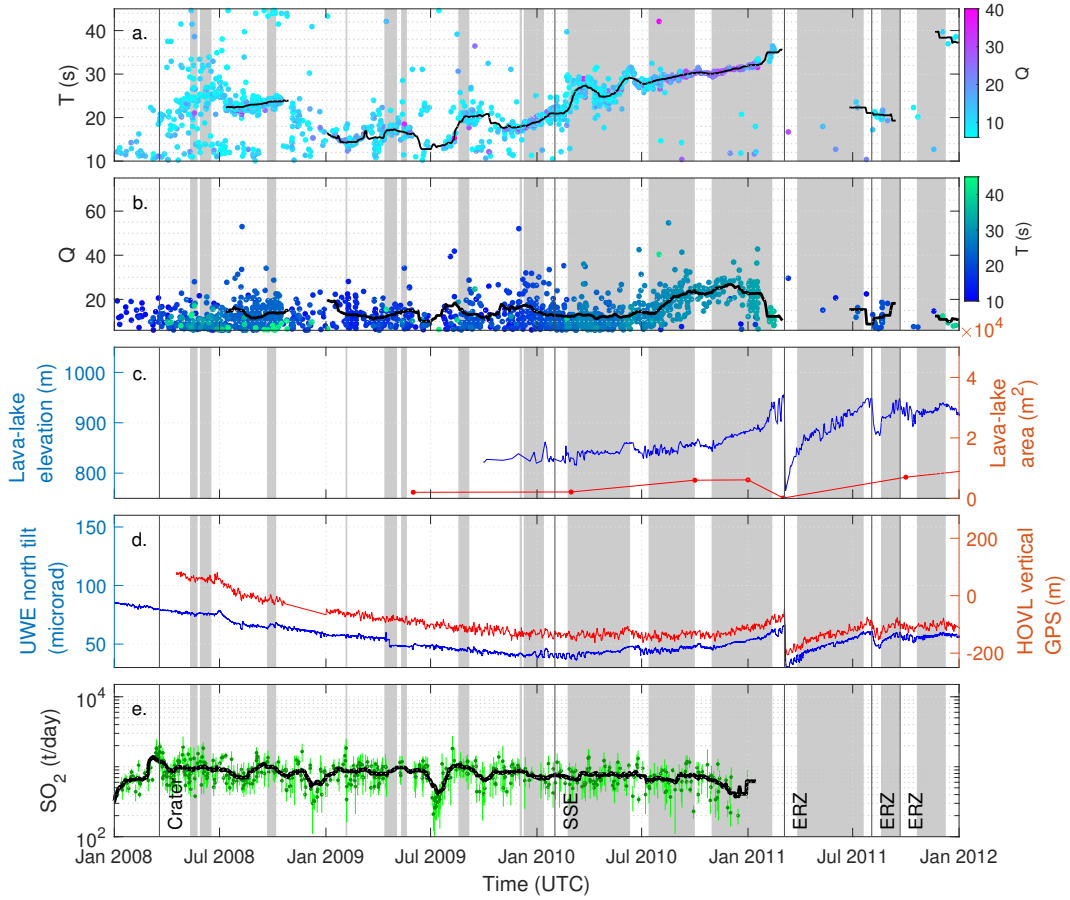


**Figure 10.** Section of the VLP catalog from 2008-2011. (a and b) Period and quality factor over time. Black lines show 30-day moving averages over the events we have labeled as potential conduit-reservoir oscillations, neglecting outliers or events from times with no consistent dominant period. (c) Lava-lake surface elevation and surface area. (d) UWE north tilt and HOVL vertical GPS. (e) Average daily  $\text{SO}_2$  (dark green dots) and standard deviations (light green lines). The black line is a 30-day moving average. ‘Crater’ indicates where the Halema‘uma‘u crater first formed, ‘SSE’ indicates slow slip events, ‘Int’ indicates documented summit intrusions, and ‘ERZ’ indicates eruptions along the East Rift Zone. Grey bars in all plots indicate times of long-term ground inflation (section 2.8).

446

### 3.1.1 Conduit-reservoir resonance

447

448

449

450

451

452

The first category of signals we term ‘conduit-reservoir oscillations’. These constitute the main trend of VLPs starting at  $T \sim 20$  s in 2010, increasing to  $\sim 40$  s in early 2011, and fluctuating between 35-43 s from 2012 until the caldera collapse onset in May 2018 (Fig. 10, 11). Some other events prior to 2010 and during the series of lava-lake draining events in 2011 may also fit into this category. The conduit-reservoir oscillation is the fundamental resonant eigenmode of the coupled conduit and shallow magma reser-

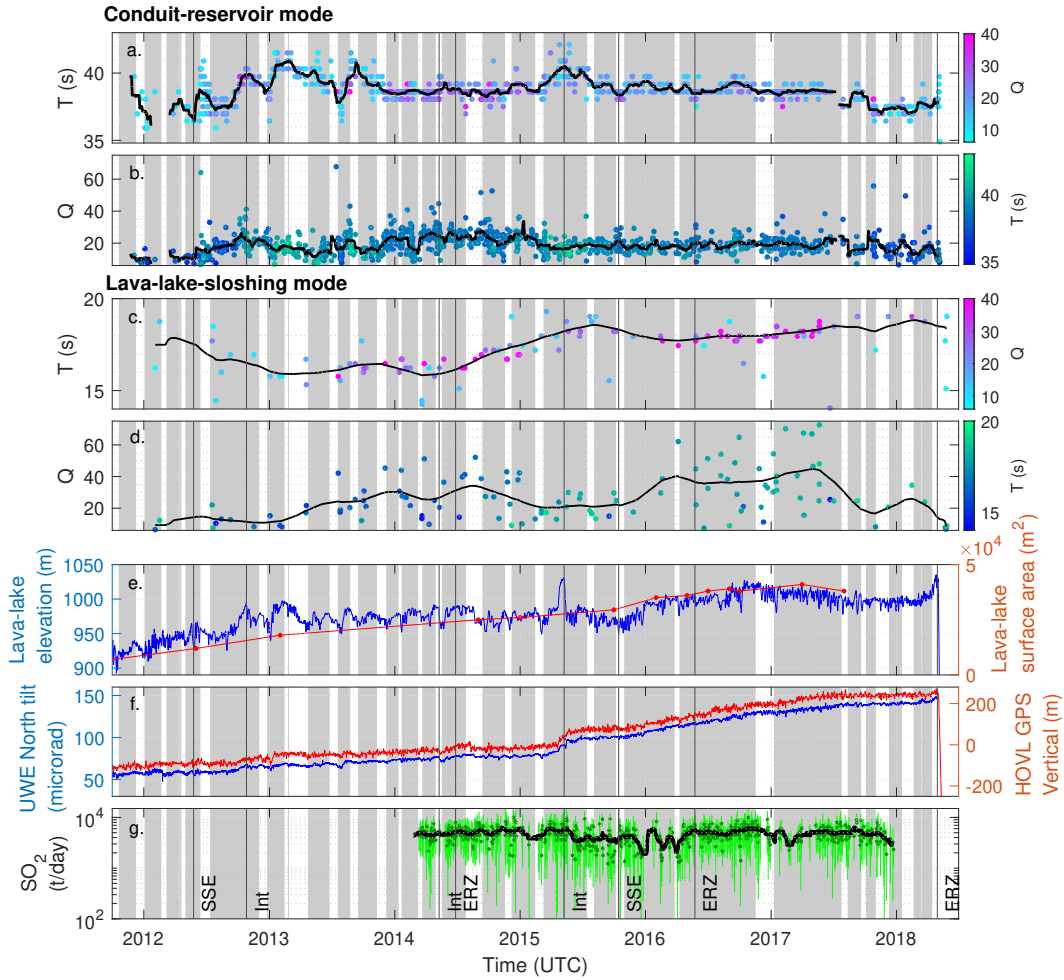


**Figure 11.** Section of the VLP catalog highlighting conduit-reservoir and lava-lake sloshing resonance from 2012-2018. (a and b) Period and quality factor of conduit-reservoir events over time. Black lines show 30-day moving average. (c and d) Period and quality factor of lava-lake sloshing over time. Black lines show 120 day moving average. (e) Lava-lake surface elevation and surface area. (f) UWE north tilt and HOVL vertical GPS. (g) Average daily  $\text{SO}_2$  (dark green dots) and standard deviations (light green lines). The black line is a 30-day moving average. ‘SSE’ indicates slow slip events, ‘Int’ indicates documented summit intrusions, and ‘ERZ’ indicates eruptions along the East Rift Zone. Grey bars in all plots indicate times of long-term ground inflation (section 2.8).

453 voir system, in which the magma column in the conduit and lava-lake oscillates verti-  
 454 cally and pushes magma in and out of the underlying reservoir (Chouet & Dawson, 2013;  
 455 Liang, Crozier, et al., 2020). Other resonances such as from Krauklis (crack) waves or  
 456 acoustic waves (organ pipe eigenmodes) are predicted to generally have higher frequen-  
 457 cies and lower amplitudes (Karlstrom & Dunham, 2016; Liang, Karlstrom, & Dunham,  
 458 2020). Restoring forces for the conduit-reservoir oscillation come from magma reservoir  
 459 compressibility (combined wall rock elasticity and multiphase magma compressibility)

460 and gravity/buoyancy, while damping primarily comes from viscous dissipation along the  
 461 conduit walls. Ground deformation during these events is primarily from uniform infla-  
 462 tion/deflation of the magma reservoir; deformation from the conduit is small by com-  
 463 parison.

464 Conduit-reservoir oscillations can be triggered/driven by a variety of different mech-  
 465 anisms, producing signals with different onset characteristics. We term conduit-reservoir  
 466 oscillations with abrupt onsets and inflationary first motions ‘Normal’; this category in-  
 467 cludes rockfall or lava-lake surface explosion triggered events and is analogous to ‘type  
 468 2’ events in Dawson and Chouet (2014). There is often high-frequency or broadband en-  
 469 ergy present at the onset of Normal events, as well as inflationary steps in tilt data (Chouet  
 470 & Dawson, 2013; Orr et al., 2013; Dawson & Chouet, 2014) (Fig. 12, S12, S13). We term  
 471 conduit reservoir oscillations with abrupt onsets and deflationary first motions ‘Reverse’;  
 472 analogous to ‘type 3’ events in Dawson and Chouet (2014) (Fig. 12). These events of-  
 473 ten do not have obvious high frequency triggers, and some exhibit deflationary tilt steps.  
 474 The trigger for Reverse events is not known, but has been proposed to involve impul-  
 475 sive magma movement at depth due to flow transients or fracture/dike opening (Dawson  
 476 & Chouet, 2014). Some conduit-reservoir events do not fit very clearly into either cat-  
 477 egory, for example those with gradual onsets or multiple step increases in oscillation am-  
 478 plitude (S12, S14).

479 Our first motion algorithm classifies 77% of conduit-reservoir events after 2012 as  
 480 Normal, 17% as Reverse, and the remaining 6% as undetermined (Fig. 13). Prior to 2012  
 481 our classifications are less reliable due to the prevalence of VLP tremor and shorter res-  
 482 onant periods (which makes phase offsets between stations less negligible). The mean  
 483 and median amplitudes of Normal events are both about twice as large as those of Re-  
 484 verse events, though both types of events exhibit variation in amplitude over orders of  
 485 magnitude (Fig. S15). We do not find any appreciable differences in distributions of  $T$   
 486 or  $Q$ , or different correlations with other datasets such as tilt and lava-lake elevation be-  
 487 tween Normal and Reverse events (Fig. S15).

### 488 **3.1.2 Lava-lake sloshing**

489 The second category of signals we term ‘lava-lake sloshing’. These have  $T$  of 10-  
 490 20 s and are recognizable from 2010-2018 in our catalog (Fig. 10, 11). Inversions of se-  
 491 lect lava-lake sloshing events by Liang and Dunham (2020) supports suggestions by Dawson  
 492 and Chouet (2014) that they are likely caused by lateral surface gravity wave resonance  
 493 in the lava-lake (i.e., ‘sloshing’). The sloshing could induce pressure perturbations at the  
 494 top of the conduit causing a forced oscillation of the conduit-reservoir system, so ground  
 495 motions could be from a combination of pressure against the lava-lake walls and reser-  
 496 voir inflation/deflation. There are some times where two distinct lava-lake sloshing sig-  
 497 nals occur with slightly different periods (Fig. 12, S12), likely representing sloshing along  
 498 different axes of the lava-lake (Dawson & Chouet, 2014; Liang & Dunham, 2020). These  
 499 are not very prevalent in our catalog at the thresholds shown, which may be partly be-  
 500 cause often one of the two signals will be too close in period to a larger lava-lake slosh-  
 501 ing signal or have too low of a signal/noise ratio to be included.

502 Around 75% of lava-lake sloshing events in our catalog appear alongside Normal  
 503 conduit-reservoir oscillations; the rest appear in isolation (Fig. 12, 13, S12, S16). That  
 504 none appeared alongside Reverse oscillations is consistent with the idea that Reverse os-  
 505 cillations are triggered from depth (Dawson & Chouet, 2014) and so the lava-lake is not  
 506 directly perturbed. It also indicates that the magma flowing in/out of the top of the con-  
 507 duct during Reverse conduit-reservoir oscillations does not induce appreciable lava-lake  
 508 sloshing, which could be due to the small volumes of magma involved and/or to the top  
 509 of the conduit not being laterally offset from the center of the lava-lake.

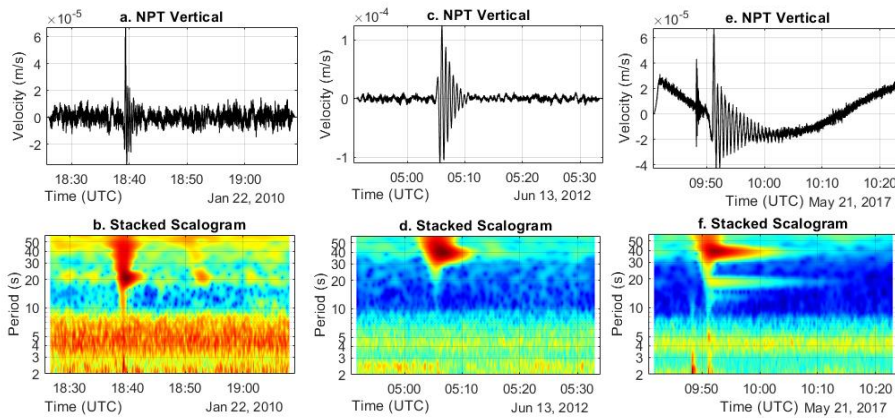


**Figure 12.** Example VLP events. (a and b) Normal conduit-reservoir oscillation event along with background VLP periodic tremor from January 2010, when the lava-lake became persistent (Patrick, Swanson, & Orr, 2019). The event had an impulsive broadband onset and inflationary first motions, indicative of a rockfall trigger. The background VLP periodic tremor had the same dominant period as the impulsively triggered VLP event, but often unclear onsets and no higher frequency triggers. (c and d) Reverse VLP event from June 2012, shortly after the May 2012 SSE. This event had an impulsive onset but no high frequency trigger. There was a small initial inflationary motion but the first large oscillation was deflationary. (e and f) Normal conduit-reservoir event with two lava-lake sloshing events from May 2017. A higher frequency impulsive signal occurred about 2 minutes before these events that may have been related to their triggering.

510

### 3.1.3 Other VLP seismicity

511

512

513

514

515

516

517

518

519

520

521

522

523

We will use the term ‘periodic tremor’ to refer to signals with clearly elevated energy in one or more relatively focused periods, but that are not obviously isolated in time and lack clear onsets and/or exponential decays. Our method will not return detections if periodic tremor amplitude is constant, but where amplitude is variable our method will consider any local amplitude maxima above the set detection thresholds. For such local maxima the apparent decay rate could be controlled by the forcing time-function rather than the inherent damping of the resonator, so estimates of  $Q$  returned by our method might not reflect the same physical properties as for impulsively triggered resonance. Periodic tremor occurs throughout the study timespan (Fig. 12, S17, S18, S19, S20, S21, S22), often with the same dominant periods as impulsively triggered conduit-reservoir or lava-lake sloshing oscillations. We thus hypothesize that the periodic tremor often represents these same resonant mechanisms with continuous rather than discrete forcing.

524

525

526

527

528

529

530

Our catalog includes some VLP oscillations that exhibit gliding-frequencies over the duration of a single event (Fig. S23, S24). These constitute many of the events in our catalog with outlier values of  $T$  (Fig. 9) and are more prevalent when a higher phase deviation threshold is used. The values of  $T$  and  $Q$  returned by our methods will not be representative of the whole signals, but visual inspection reveals that gliding-frequency VLP oscillations are present at various times throughout the studied timespan and with various starting and ending periods and durations. Gliding-frequencies have been pre-

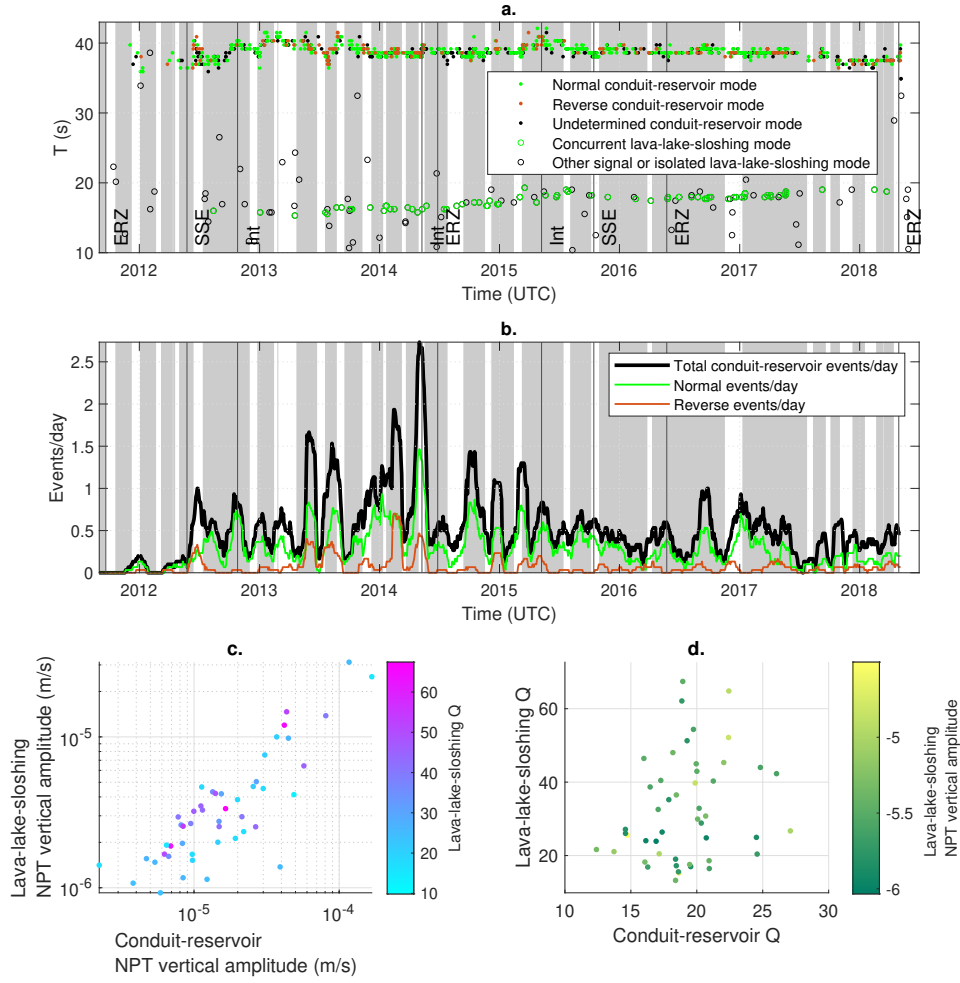


**Figure 13.** (a) Onset polarity (Normal or Reverse) of conduit-reservoir oscillations and lava-lake sloshing that occurred alongside a detected conduit-reservoir event. (b) Conduit-reservoir event density calculated over 30-day windows. We note that event density will vary by orders-of-magnitude depending upon the event detection thresholds used (section 2.6), so is most useful for comparing relative event densities through time. ‘Crater’ indicates where the Halema‘uma‘u crater first formed, ‘SSE’ indicates slow slip events, ‘Int’ indicates documented summit intrusions, and ‘ERZ’ indicates eruptions along the East Rift Zone. Grey bars in plots a and b indicate times of long-term ground inflation (section 2.8). (c) amplitudes (from vertical velocity at station NPT) of conduit-reservoir oscillations vs corresponding lava-lake sloshing. (d) Quality factor of conduit-reservoir oscillations vs corresponding lava-lake sloshing.

531 viously identified in tremor at Kīlauea, but at much higher frequencies (0.6-6 Hz) and  
 532 with gliding occurring over hours-days (Unglert & Jellinek, 2015). In some cases, the gliding-  
 533 frequency VLP oscillations appear to start or end at similar periods to non-gliding conduit-  
 534 reservoir or lava-lake sloshing oscillations, indicating that at least some of them may be  
 535 related to these other oscillations. Some may represent rising bubble slugs, which could  
 536 create a varying oscillation period during ascent and then possibly trigger standard de-

537 caying conduit-reservoir resonance after bursting at the surface (e.g., James et al., 2008;  
 538 Chouet et al., 2010). Alternately, some may represent examples of either conduit-reservoir  
 539 or lava-lake sloshing resonance where magma properties change over the course of the  
 540 resonance. This could occur if the perturbation that induces resonance destabilizes some  
 541 aspect of the shallow magma system, such as by causing collapse of a foam layer in the  
 542 lava-lake or upward movement of a bubble slug or bubble cloud.

543 **3.2 Correlations among datasets**

544 Here we analyze correlations between the various geophysical datasets, conduit-reservoir  
 545 oscillation properties, and lava-lake sloshing properties. Fig. 14 shows correlations over  
 546 the 2008-2018 timespan (see Fig. S25 for just the 2012-2018 timespan). When looking  
 547 over such long timescales only a few strong correlations are apparent. Fig. 15 shows mov-  
 548 ing 90-day correlations, which reveals more correlations between datasets but that these  
 549 correlations change over time.

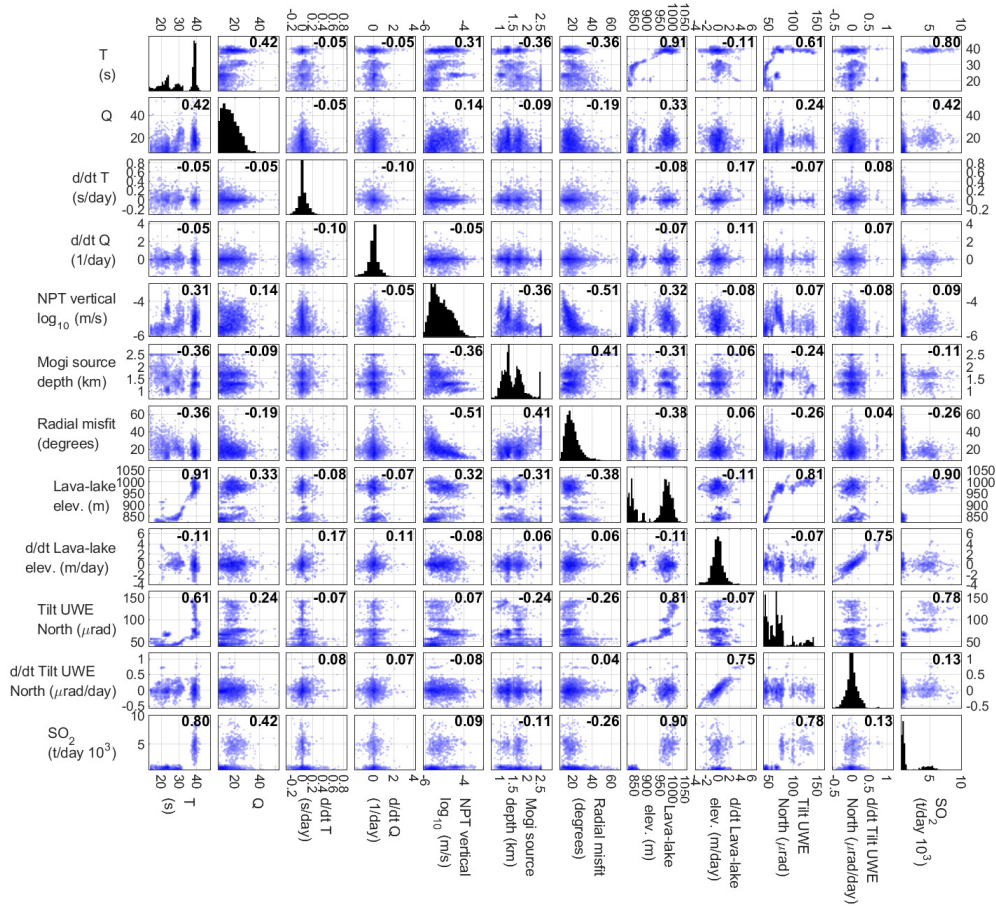


**Figure 14.** Conduit-reservoir oscillation correlation matrices from 2008-2018 (see Fig. S25 for just the 2012-2018 timespan). Off-diagonal plots are shaded by the logarithm of the number of points in each parameter bin, and histograms on diagonal plots show the distribution of each parameter. Numbers are Pearson’s correlation coefficients, only shown for correlations with P-values less than 0.05. All time derivatives, indicated by ‘d/dt’, were calculated with a 7-day cutoff-period differentiator filter.

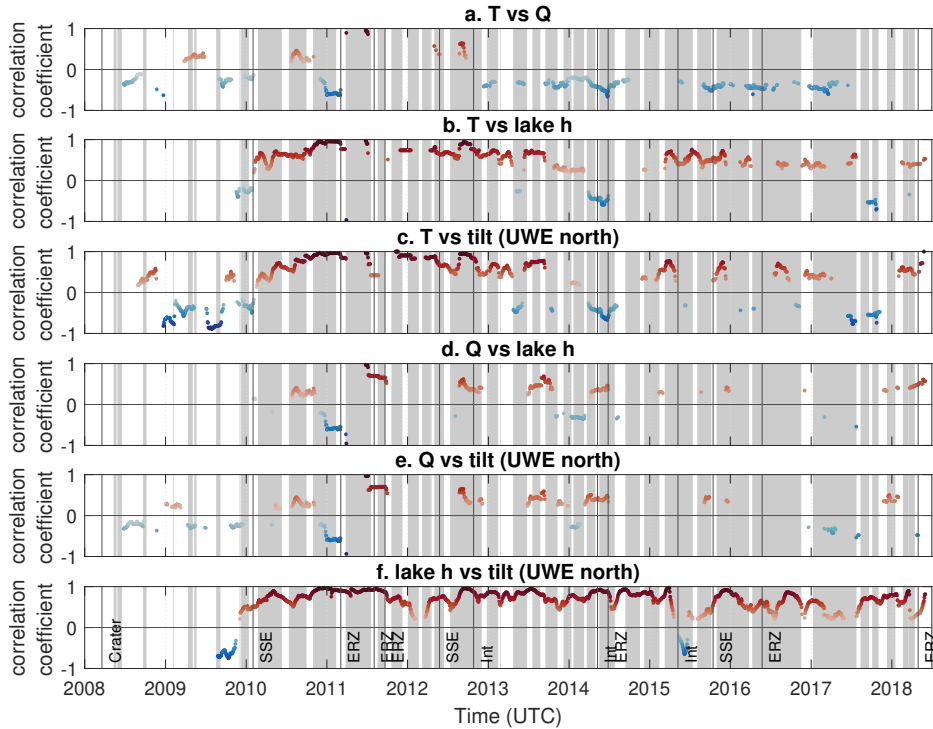


**Figure 15.** Conduit-reservoir oscillation Pearson’s correlation coefficients calculated over moving 90-day windows. Windows with p-values greater than 0.05 were excluded. Red and blue highlight positive and negative correlations, respectively. ‘SSE’ indicates slow slip events, ‘Int’ indicates documented summit intrusions, and ‘ERZ’ indicates eruptions along the East Rift Zone. Grey bars in the all plots indicate times of long-term ground inflation (section 2.8).

### 550 3.2.1 Ground deformation and lava-lake elevation correlation

551 Ground surface deformation data from near field tilt-meters and GPS stations indicates the rate of ground inflation/deflation of the Kilauea summit region. This primarily reflects pressure in the shallow summit reservoir, but may also be influenced by pressure in the proposed deeper south caldera reservoir or motion of the south flank (e.g., Owen et al., 2000; Baker & Amelung, 2012; Anderson et al., 2015). Lava-lake elevation has previously been shown to be correlated with ground inflation on timescales of hours or more, including during so-called deflation-inflation events, though not during some shorter-duration fluctuations in lava-lake elevation related to gas-pistoning (e.g., Patrick et al., 2015; Anderson et al., 2015; Patrick, Orr, Swanson, & Lev, 2016; Patrick, Swanson, & Orr, 2019). This correlation is present over most of the 2008-2018 timespan, with a 0.8 overall correlation coefficient (Fig. 14, 15, S25). The correlation implies that lava-lake elevation is analogous to a Pitot tube for the summit magma reservoir and responds proportionally to changes in reservoir pressure.

564 However, this relation is not constant as evidenced by both the non-linear relationship between lava-lake elevation and tilt (Fig. 14) and the variation in local correlation coefficients from almost 1 to negative values (Fig. 15). This indicates that the Pitot tube relation between ground inflation and lava-lake elevation changes over time. We believe that these deviations reflect superposition of processes on different characteristic timescales. For example, in early 2017 ground inflation and lava-lake elevation are positively correlated on day-month long timescales, but there is a long-term ground inflation trend

571 despite average lava-lake elevation remaining constant (Fig. 11). There are also abrupt  
 572 events that change the relation between ground inflation and lava-lake elevation, such  
 573 as the May 2015 intrusion (Fig. 11).

### 574 **3.2.2 Conduit-reservoir resonance correlations**

575 During most of the timespan conduit-reservoir oscillation  $T$  and  $Q$  exhibit a weak  
 576 negative correlation, with an overall correlation coefficient of -0.06 but local correlation  
 577 coefficients often around -0.7 (Fig. 14, 15, S25). There are isolated times where  $T$  and  
 578  $Q$  are positively correlated, such as in mid-2010 (correlation coefficient near 1) and mid-  
 579 2012 (correlation coefficient around 0.7) (Fig. 10, 11, 15).

580 Conduit-reservoir oscillation  $T$  is positively correlated with lava-lake elevation dur-  
 581 ing most of the timespan, with correlation coefficients mostly between 0.3 and 1 (Fig.  
 582 15), and a weak overall correlation coefficient of 0.11 (Fig. 14, S25). However, there are  
 583 times with negative local correlations, such as around the 2014 Pu'u 'Ō'ō eruption (cor-  
 584 relation coefficient around -0.6), and in late 2017 (correlation coefficient around -0.7).  
 585 The correlation between  $T$  and ground inflation (i.e., tilt) exhibits a similar trend to the  
 586 correlation between  $T$  and lava-lake elevation after the arrival of a persistent lava-lake  
 587 in late 2009, and exhibits a variable but mostly negative trend prior to this (Fig. 14, 15,  
 588 S25). Conduit-reservoir  $T$  is positively correlated with event amplitude, even when con-  
 589 sidering only vertical velocity (which should not be sensitive to instrument tilt) (Fig. 14,  
 590 S25).

591 Conduit-reservoir oscillation  $Q$  exhibits much less consistent correlations with ground  
 592 inflation and/or lava-lake elevation than  $T$  does (Fig. 14, 15, S25). Throughout much  
 593 of the studied timeline there is no significant correlation between  $Q$  and either dataset.  
 594 There are several isolated time-segments such as June-September 2011 where  $Q$  is pos-  
 595 itively correlated with ground inflation and lava-lake elevation, and one time-segment  
 596 from December 2010 to March 2011 with a significant negative correlation (Fig. 15).

597 We find increases in both conduit-reservoir event density and  $T$  around the inferred  
 598 October 2012 and May 2015 intrusions. There is no obvious change in  $Q$  corresponding  
 599 to either intrusion, though the correlation between  $T$  and  $Q$  does change from positive  
 600 to negative at the October 2012 intrusion (Fig. 9, 15). Perhaps surprisingly, neither in-  
 601 trusion appears to correspond to changes in ground motion patterns (Fig. 16).

602 ERZ eruptions for which we detect conduit-reservoir oscillations both before and  
 603 after the events (i.e., the June 2014 and May 2016 Pu'u 'Ō'ō eruptions) do not obviously  
 604 relate to changes in conduit-reservoir oscillation  $T$  or  $Q$ . However, sharp changes in the  
 605 correlations between  $T$  and  $Q$ ,  $T$  and lava-lake elevation/tilt, and  $Q$  and lava-lake ele-  
 606 vation/tilt occur alongside the June 2014 eruption, and more subtle changes in these cor-  
 607 relations may also be present alongside the May 2016 eruption (Fig. 9, 15). Interestingly,  
 608 there are changes in ground motion patterns following both eruptions that are readily  
 609 apparent in the time-series of Mogi source inversions and vertical/horizontal velocity ra-  
 610 tios (Fig. 16).

### 611 **3.2.3 Lava-lake sloshing correlations**

612 Due to the sparsity of well-characterized lava-lake sloshing events it is difficult to  
 613 robustly examine correlations with other other datasets on timescales of months or less.  
 614 Long-term average lava-lake sloshing  $T$  increased over most of the timespan, except for  
 615 during 2012 (when lava-lake sloshing events were sparse and exhibited large scatter in  
 616  $T$ ) and a clear decrease during late 2015. The long-term increase in  $T$  roughly corresponds  
 617 to an observed long-term increase in lava-lake surface area, and the decrease in lake 2015  
 618 roughly corresponds to a several month long decrease in average lava-lake elevation. Lava-  
 619 lake sloshing  $Q$  exhibits large scatter over most of the timespan, with the exception of

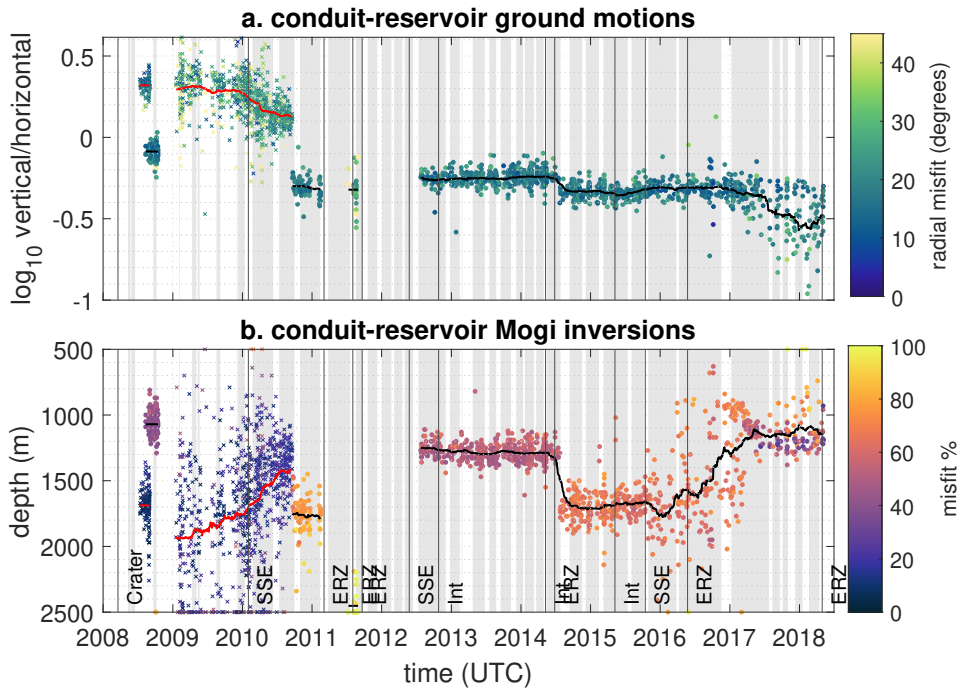


**Figure 16.** Ground motion patterns and Mogi spherical reservoir source inversions for conduit-reservoir oscillations. Dots and black lines indicate events and 120-day moving averages for times with more than 6 stations available. Crosses and red lines indicate events and 120-day moving averages for times with only one station available, so ground motion patterns are poorly constrained and should not be directly compared to events with more stations. Depths are relative to the caldera floor. ‘Crater’ indicates where the Halema‘uma‘u crater first formed, ‘SSE’ indicates slow slip events, ‘Int’ indicates documented summit intrusions, and ‘ERZ’ indicates eruptions along the East Rift Zone. Grey bars in all plots indicate times of long-term ground inflation (section 2.8).

620 during 2012 when  $Q$  was generally less than 20, and during 2015 when  $Q$  was generally  
 621 between 10 and 30. There is a roughly linear relation between conduit-reservoir oscil-  
 622 lation amplitude and lava-lake sloshing amplitude, though with an appreciable amount  
 623 of scatter (Fig. 13). Lava-lake sloshing  $Q$  does not appear to be correlated with conduit-  
 624 reservoir oscillation  $Q$  (Fig. 13), which could indicate that some properties that govern  
 625 damping of the two resonant modes vary independently.

## 626 4 Discussion

627 Our new catalog of VLP seismic events provides an outstanding tool both to docu-  
 628 ment the progression of a long-lived (10 year) open vent eruptive episode at Kilauea  
 629 Volcano and probe shallow magma plumbing system geometry and magma properties  
 630 through time. In the following discussion we highlight how simple physical models for  
 631 the resonant oscillations identified in Kilauea seismic data may be used to understand  
 632 some of the trends observed in the 2008-2018 eruptive sequence. We also identify obser-  
 633 vations that are not well explained by current models and that point to next steps for

634 understanding VLP seismicity at Kīlauea. Lastly, we interpret the 2008-2018 timeline  
 635 of VLP seismicity with insights from the resonance models and other datasets and ob-  
 636 servations.

#### 637 4.1 Interpreting changes in conduit-reservoir resonance

638 The conduit-reservoir oscillator model of Liang, Karlstrom, and Dunham (2020),  
 639 which extends earlier work by (Chouet & Dawson, 2013), provides estimates of  $T$  and  
 640  $Q$  assuming a cylindrical conduit and isothermal conditions, and neglecting inertia and  
 641 viscous drag in the overlying lava-lake and compressibility of magma in the conduit. The  
 642 inviscid conduit-reservoir resonance period is:

$$T_0 = 2\pi \sqrt{\frac{L_c \bar{\rho}_c}{\Delta \rho_c g \sin \alpha + A_c C_t^{-1}}}. \quad (9)$$

643 where  $L_c$  is conduit length,  $\bar{\rho}_c$  is average magma density in the conduit,  $\Delta \rho_c$  is density  
 644 difference between the bottom and top of the conduit,  $\alpha$  is conduit dip angle,  $A_c$  is con-  
 645 duct cross-sectional area, and  $C_t$  is total reservoir storativity (from both magma com-  
 646 pressibility and elastic reservoir stiffness). With viscous damping included,  $T$  and  $Q$  de-  
 647 pend upon  $T_0$  as well as a momentum diffusion timescale:

$$\tau_{visc} = \frac{R_c^2 \bar{\rho}_c}{\mu_c}, \quad (10)$$

648 where  $R_c$  is conduit radius and  $\mu_c$  is average magma viscosity. Liang, Karlstrom, and  
 649 Dunham (2020) detail the full governing equations and numerical methods used to solve  
 650 for  $T$  and  $Q$ .

651 This model involves a number of simplifications that limit its applicability for a de-  
 652 tailed analysis of Kīlauea VLP seismicity and its observed relations to other datasets over  
 653 time. Lava-lake elevation, which is strongly correlated with  $T$  at many times (Fig. 15),  
 654 is not considered in this model. Inertia and viscous drag in the lava-lake might affect re-  
 655 sonance, as could non-cylindrical conduit/lava-lake geometries, non-Newtonian magma  
 656 rheology, and bubble growth and resorption (e.g., Karlstrom & Dunham, 2016) in the  
 657 magma reservoir. Lastly, incorporating a background state model for density/viscosity  
 658 profiles of the multiphase magma contained within the conduit-reservoir system based  
 659 on known magma physics, chemistry, and outgassing dynamics would greatly enhance  
 660 the applicability of the model. This could range from simple magmatic cases (e.g.,  
 661 Karlstrom & Dunham, 2016) to considering exchange flow (e.g., Fowler & Robinson, 2018).  
 662 This would allow changes in  $T$  and  $Q$  to be related to volcanologically important pro-  
 663 cesses such as inputs of new melt/volatiles and changes in magma convection regimes.  
 664 This would also allow comparison with summit gas datasets and inform how the magma  
 665 density profile in the conduit shifts with lava-lake elevation and/or reservoir pressure,  
 666 which likely plays a role in the observed correlations with these datasets. Implement-  
 667 ing a model with these improvements is beyond the scope of this project, but the model  
 668 of Liang, Karlstrom, and Dunham (2020) can still help interpret some of the observa-  
 669 tions from this VLP seismicity catalog.

670 Liang, Crozier, et al. (2020) conducted stochastic inversions for 4 events from 2008-  
 671 2013, and favor a geometry consisting of a spherical reservoir with a centroid  $\sim 1.4$  km  
 672 beneath the vent and a radius of  $\sim 1$  km, resulting in a conduit length of a few hundred  
 673 meters. In this regime  $T$  and  $Q$  are controlled by conduit geometry and magma prop-  
 674 erties in the conduit, and have minimal sensitivity to reservoir compressibility (Fig. 17).  
 675 However, the inversions show that there are many trade-offs that make uniquely constrain-  
 676 ing model parameters for a given event difficult without additional constraints. Fig. 17  
 677 illustrates this problem:  $T$  and  $Q$  vary with multiple unknown parameters that likely co-  
 678 vary in different ways and on differing timescales. The inversions do show probable dif-  
 679 ferences in both magma properties (density, density contrast, and viscosity) and in magma

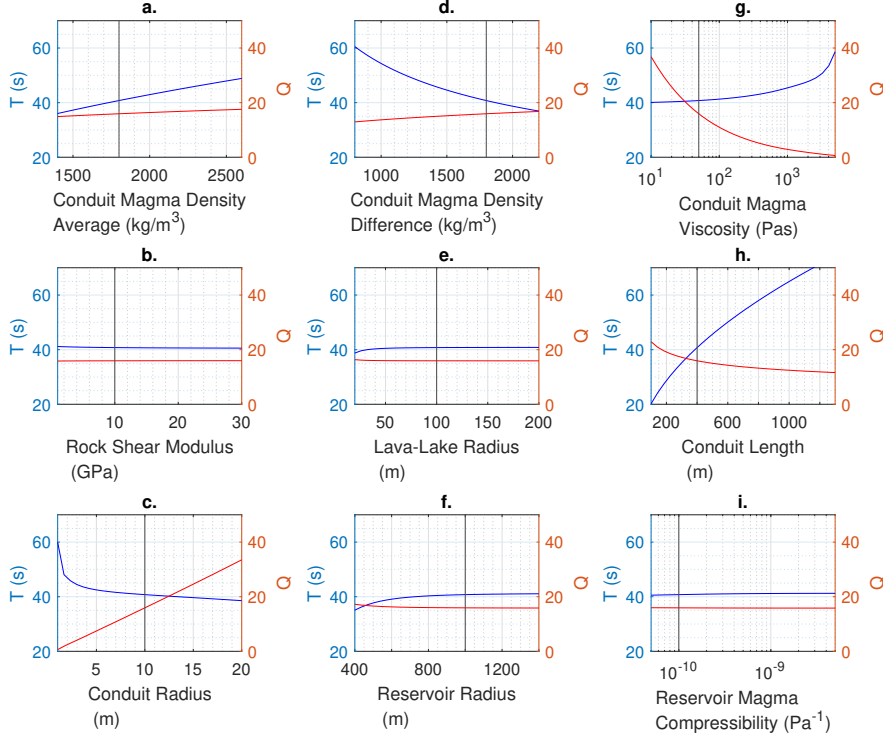


**Figure 17.** (a-i) Predicted variation in  $T$  and  $Q$  due to varying each model parameter in isolation in the conduit-reservoir resonance model of Liang, Karlstrom, and Dunham (2020) (Eq. 9-10), assuming a spherical reservoir geometry. Black lines indicate the default value used for each parameter.

680  
681

system geometry (conduit length and radius) between the four events selected, though there is significant overlap of the probability density functions for these parameters.

682  
683  
684  
685  
686  
687  
688  
689  
690  
691

Even robustly constraining the Kilauea shallow magma reservoir geometry at a given time is difficult, as indicated by the scatter in even the simple metrics shown in Fig. 16 and by the uncertainty and/or differing results obtained in previous seismic and geodetic inversions. Some previous seismic studies have inferred a source consisting of intersecting dikes (Chouet & Dawson, 2011, 2013), and multiple previous seismic and geodetic studies have supported a spherical or ellipsoidal reservoir geometry (Baker & Amelung, 2012; Anderson et al., 2015; Anderson & Poland, 2016; Liang, Crozier, et al., 2020; Anderson et al., 2019). We have not shown source models such as dikes or ellipsoids since inversions with these more complex source models for single frequency components of these VLP events are often not well constrained (Crozier et al., 2018).

692

#### 4.1.1 Short timescales

693  
694  
695  
696  
697

One way to reduce the number of free parameters is to focus on short timescales (hours-months), where it is probably reasonable to assume that the geometry of the system remains relatively constant except possibly at the few isolated times where abrupt changes in ground motion patterns occur (Fig. 16). Variation in  $T$  and  $Q$  on these short timescales is thus most likely related to changes in magma properties. Figure 17 shows

698 that of these magma properties,  $T$  is most sensitive to average magma density and magma  
 699 density difference. Assuming reasonable values for other model parameters based off the  
 700 inversions of Liang, Crozier, et al. (2020), variation in either density parameter of  $\sim 500 \text{ kg/m}^3$   
 701 would be required to explain the observed month-scale variability in  $T$  of up to  $\sim 6 \text{ s}$  (e.g.,  
 702 July-September 2013, Fig. 11). Similarly, the day-scale variability in  $T$  of up to  $\sim 3 \text{ s}$  would  
 703 require changes in either density parameter of  $\sim 250 \text{ kg/m}^3$ .  $Q$  is most sensitive to magma  
 704 viscosity (Fig. 17). Variation in magma viscosity of up to an order of magnitude would  
 705 be required to explain the observed day-month timescale variability in  $Q$  of up to a factor  
 706 of four (e.g., Feb-April 2014, Fig. 11).

707 At many times there is a negative correlation between  $T$  and  $Q$  (Fig. 15). This could  
 708 be produced by either isolated changes in magma density difference, magma viscosity,  
 709 conduit radius, or conduit length, or by changes in various combinations of parameters  
 710 (Fig. 17). There are also times where  $T$  and  $Q$  are positively correlated (Fig. 15). Con-  
 711 duct average magma density is the only parameter that could produce this in isolation,  
 712 though since the effect of average magma density on  $Q$  is very minor the positive correla-  
 713 tions more likely indicate changes in some parameter combinations. For example, in-  
 714 creasing average magma density or decreasing magma density difference while decreas-  
 715 ing magma viscosity would result in a net increase in both  $T$  and  $Q$ .

#### 716 **4.1.2 Magma properties**

717 Variation in magma density in the Kīlauea shallow magma system primarily re-  
 718 flects changes in porosity, which is controlled by volatile contents, pressure, and temper-  
 719 ature. In general, producing high porosities deeper in the conduit will require large amounts  
 720 of volatiles since both volatile solubility and gas density increase with increasing pres-  
 721 sure (e.g., Gonnermann & Manga, 2007; Iacono-Marziano et al., 2012). We show magma  
 722 density as a function of volatile contents and pressure in Fig. 18 plot j. These densities  
 723 are calculated using the average Kīlauea glass composition from Edmonds et al. (2013)  
 724 and the  $\text{H}_2\text{O-CO}_2$  solubility model of Iacono-Marziano et al. (2012). At 1 MPa ( $\sim 50$ -  
 725 100 m deep) the required  $500 \text{ kg/m}^3$  change in density could arise from a two-fold in-  
 726 crease in  $\text{H}_2\text{O}$  or  $\text{CO}_2$ , while at 10 MPa ( $\sim 500$ -1000 m deep) this change would require  
 727 a four-fold or more increase in  $\text{H}_2\text{O}$  or  $\text{CO}_2$ . Estimates of primitive (or ‘parent’) magma  
 728 volatile contents are variable from 0.5-1 wt%  $\text{CO}_2$ , 0.4-0.7 wt%  $\text{H}_2\text{O}$ , and up to 0.18 wt%  
 729 sulfur (Edmonds et al., 2015). However, different amounts of volatiles may be present  
 730 at a given depth due to disequilibrium degassing (e.g., volatile accumulation or deple-  
 731 tion due to gas fluxing and/or magma convection) since  $\text{CO}_2$  begins exsolving well be-  
 732 neath the shallow reservoir and  $\text{H}_2\text{O}$  and sulfur will generally begin exsolving around  
 733 the shallow reservoir or conduit (e.g., Iacono-Marziano et al., 2012; Edmonds et al., 2015).

734 Variation in apparent magma viscosity (melt + bubbles) could be due to chang-  
 735 ing porosity (the effects of which depend upon flow regime), dissolved  $\text{H}_2\text{O}$  concentra-  
 736 tion, melt temperature, and crystal contents (e.g., Llewellyn & Manga, 2005; Giordano  
 737 et al., 2008; Mader et al., 2013). We show how apparent magma viscosity  $\mu$  might vary  
 738 in response to temperatures and porosity in Fig. 18 plot k. We calculate melt viscosity  
 739  $\mu_l$  from the model of Giordano et al. (2008) using the average Kīlauea glass composi-  
 740 tion from Edmonds et al. (2013), then apply the low capillary-number model from Llewellyn  
 741 and Manga (2005) to account for porosity  $\phi$ :

$$\mu = (1 - \phi)^{-1} \mu_l \quad (11)$$

742 Porosity alone will generally only change viscosity by up to a factor of three, so the re-  
 743 quired order of magnitude changes likely also involve changes in temperature on the or-  
 744 der of 100 C or significant changes in crystal contents (e.g., Mader et al., 2013).

745 Changes in convective regimes could cause changes in volatile contents, crystal con-  
 746 tents, and melt temperature (e.g., Witham & Llewellyn, 2006; Harris, 2008; Fowler & Robin-  
 747 son, 2018). For example, a single convective cell extending from the lava-lake surface though

748 the conduit might result in lower average magma temperatures in the conduit than sep-  
 749 arate convective cells in the lava-lake and conduit (Patrick, Orr, Swanson, & Lev, 2016).  
 750 Injections of new volatiles and/or melt from depth, or changes in the background volatile/melt  
 751 supply rate, could impact both temperature and volatile contents on various timescales.  
 752 Stokes rise velocity of bubbles with radii of 1-100 mm are 0.01 mm/s-1 m/s, and sim-  
 753 ulations of bubble slugs show ascent velocities on the order of 1 m/s (Chouet et al., 2010).  
 754 Based on inferred magma upwelling rates in the lava-lake of 0.15-0.3 m/s, circulation timescales  
 755 in the lava-lake would be on the order of hours (Patrick, Orr, Swanson, & Lev, 2016).  
 756 So volatile rise timescales through the conduit/lava-lake for large bubbles could be on  
 757 the order of minutes, whereas smaller bubbles will mostly move by convecting with the  
 758 surrounding melt. Shallowly-driven processes such as gas pistoning or foam buildup likely  
 759 also contribute to changes in volatile contents on timescales of minutes-days (e.g., Nadeau  
 760 et al., 2014; Patrick, Orr, Sutton, et al., 2016; Patrick, Swanson, & Orr, 2019).

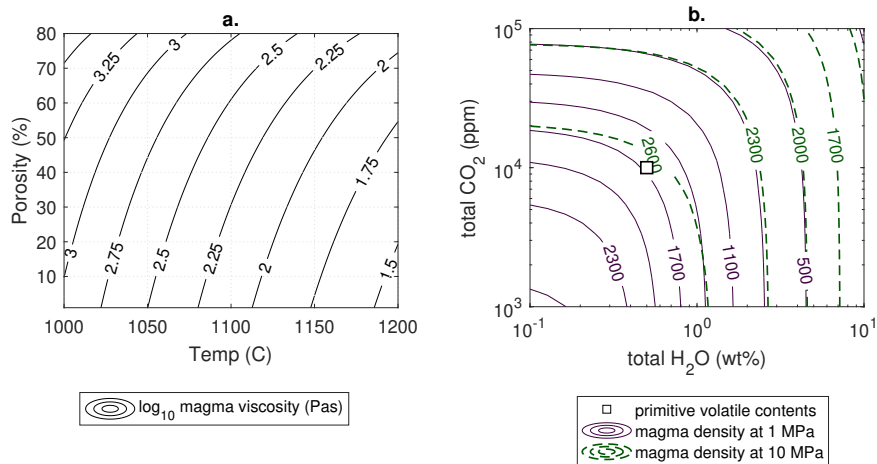


**Figure 18.** (a) Apparent magma viscosity as a function of temperature and porosity (section 4.1). (b) Magma density as a function of H<sub>2</sub>O and CO<sub>2</sub> contents at two pressures (1 and 10 MPa correspond to magmastatic depths of 40-100 m and 0.4-1 km respectively) and an assumed temperature of 1100 C (section 4.1). The density of pure melt is  $\sim 2650$  kg/m<sup>3</sup>. Estimates of primitive (or ‘parent’) magma volatile contents are from Edmonds et al. (2015).

## 761 4.2 Interpreting changes in lava-lake sloshing

762 The lava-lake sloshing events at Halema‘uma‘u have previously been interpreted  
 763 from models for surface gravity wave resonance of inviscid and incompressible fluid in  
 764 a cylindrical or wedge-shaped tank (Dawson & Chouet, 2014; Liang & Dunham, 2020).  
 765 The Halema‘uma‘u crater geometry has changed over time but remained roughly cylin-  
 766 drical (Patrick, Swanson, & Orr, 2019), though with semi-diameters that are different  
 767 enough to produce two concurrent sloshing signals with slightly different periods (Dawson  
 768 & Chouet, 2014; Liang & Dunham, 2020). The crater walls are also slightly inward dip-  
 769 ping, but the analysis of Liang and Dunham (2020) indicates that this dip will not pro-  
 770 duce appreciably different inviscid sloshing periods than vertical walls.

771 Studies of viscous incompressible fluid sloshing indicate that  $T$  and  $Q$  depend on  
 772 fluid density, fluid viscosity, and tank geometry (e.g., Bauer, 1981; Ibrahim, 2005). Due  
 773 to the presence of bubbles, a solidified surface crust, and possible foam layers under the  
 774 crust, magma in the Halema‘uma‘u lava-lake will generally be both compressible and strat-

775 ified (e.g., Carbone et al., 2013; Patrick, Orr, Sutton, et al., 2016; Poland & Carbone,  
 776 2016). The surface crust will not always act as a fully rigid or elastic cap since videos  
 777 of rockfall-triggered lava-lake sloshing show that the crust sometimes disintegrates/overturns  
 778 following event onsets (Orr et al., 2013; USGS, 2020), but it may still impact sloshing  
 779 dynamics for some events. An isotropic component of deformation found in previous in-  
 780 versions by Liang and Dunham (2020) suggests that the lava-lake sloshing drives magma  
 781 in and out of the underlying conduit/reservoir, so viscous dissipation from the conduit  
 782 may also be important. The degree of coupling between lateral fluid motions in the lava-  
 783 lake and vertical fluid motions in the conduit will depend on the offset of the top of the  
 784 conduit along the lava-lake sloshing axis, and thus on the direction of lava-lake sloshing.  
 785 Detailed analysis and inversions for  $T$  and  $Q$  for lava-lake sloshing events would require  
 786 modeling that can account for all these factors and is self-consistently coupled to the conduit-  
 787 reservoir resonance. However, we can still gain some new insights from our timeline of  
 788 lava-lake sloshing events using existing models for viscous sloshing in an isolated tank.

789 We assume a cylindrical crater geometry, for which analytical solutions for viscous  
 790 sloshing of an incompressible fluid are available. The period for the fundamental slosh-  
 791 ing eigenmode is given by (Case & Parkinson, 1957; Ibrahim, 2005):

$$T = 2\pi \left( \frac{jg}{R_L} \tanh \left( \frac{jh_L}{R_L} \right) \right)^{-1/2} \quad (12)$$

792 where  $R_L$  is lava-lake radius,  $h_L$  is lava-lake depth,  $\rho_L$  is magma density in the lava-lake,  
 793 and  $j$  is the Bessel root that satisfies  $\partial J_1(jr)/\partial r|_{r=R_L} = 0$ . Except when the lava-lake  
 794 is very shallow  $Q$  is controlled by viscous damping from the lava-lake sidewalls:

$$Q = 2\pi R_L \sqrt{\frac{2\rho_L}{\omega_L \mu_L}} \left( \frac{1 + (jR_L)^{-2}}{1 - (jR_L)^{-2}} - \frac{2jH_L}{\sinh(2jH_L)} \right)^{-1} \quad (13)$$

795 where  $\mu_L$  is magma viscosity in the lava-lake; the additional terms for viscous damping  
 796 from the tank bottom and the fluid free surface are shown in Case and Parkinson (1957).  
 797 Figure 19 shows the effect of the model parameters on  $T$  and  $Q$ .

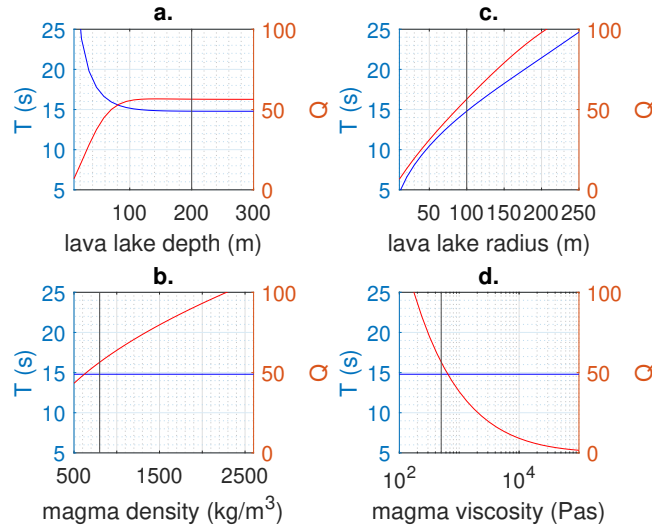


**Figure 19.** (a-d) Predicted variation in  $T$  and  $Q$  due to varying each model parameter in isolation in the viscous cylindrical tank model of (Case & Parkinson, 1957) (Eq. 12-13). Black lines indicate the default value used for each parameter.

798 The long-term increase in  $T$  is roughly consistent with the observed increases in  
 799 lava-lake diameter according to Eq. 12 (Fig. 11, 19). On shorter timescales (months or  
 800 less), the crater geometry should be relatively constant, though the effective lava-lake  
 801 surface diameter could change slightly with changing lava-lake height due to the irreg-  
 802 ular crater shape (Patrick, Swanson, & Orr, 2019), which might explain the decrease in  
 803  $T$  in late 2015. Lava-lake sloshing  $T$  does exhibit variability of up to  $\sim 3$  s on timescales  
 804 of months or less (Fig. 11), though part of this is from sloshing along different axes of  
 805 the lava-lake which detailed seismic inversions and/or video of the lava-lake could help  
 806 resolve (Liang & Dunham, 2020).

807 Lava-lake sloshing exhibits variation in average  $Q$  by up to a factor of four on timescales  
 808 of years (Fig. 11), and similar variability on timescales of days-weeks. Changes in lava-  
 809 lake depth should have a relatively minimal effect on  $Q$  except when the lava-lake is very  
 810 shallow. Additionally, since many events with similar lava-lake elevation have very dif-  
 811 ferent  $Q$  (Fig. 11), we expect other factors are primary drivers of much of the variation  
 812 in  $Q$ . For a density of  $1000 \text{ kg/m}^3$ , depth of 200 m, and radius of 100 m, producing the  
 813 observed values of  $Q$  requires viscosities ranging from  $\sim 400$ - $8000$  Pas (Fig. 19). The higher  
 814 end of this viscosity range could likely only be produced by magma cooler than  $\sim 1000$  C  
 815 (Fig. 18), which is appreciably less than geochemically inferred temperatures of 1160-  
 816 1300 C (Edmonds et al., 2013). Low magma temperatures are expected near the lava-  
 817 lake surface, where the solid crust temperatures are often  $\sim 300$  C, but temperatures should  
 818 increase with depth in a manner dependent upon the convective regime (Patrick, Orr,  
 819 Swanson, & Lev, 2016). The model used here has no vertical stratification, so does not  
 820 indicate the sensitivity of  $Q$  to viscosity as a function of depth. However, it is likely that  
 821 variation in magma properties with depth in the lava-lake is required to explain the ob-  
 822 served variation in  $Q$ .

823 For the same forcing mechanism (e.g., rockfall) and forcing location, if everything  
 824 else is constant we would expect a linear relationship between lava-lake sloshing ampli-  
 825 tude and conduit-reservoir oscillation amplitude for small amplitude perturbations. The  
 826 observed scatter could be caused by variable forcing location or mechanism, changes in  
 827 the shallow magma system geometry, or changes in magma properties in the lava-lake  
 828 or in the conduit-reservoir system. The lack of observed correlation between  $Q$  of conduit-  
 829 reservoir oscillations and  $Q$  of lava-lake sloshing (Fig. 13), which is also apparent at short  
 830 (months or less) timescales (Fig. 11), suggests that magma properties in the lava-lake  
 831 and conduit may be largely decoupled. Changes in porosity alone will generally not cause  
 832 order of magnitude changes in magma viscosity (Fig. 18), so appreciably different magma  
 833 temperatures in the conduit and lava-lake at various times may be required to explain  
 834 the large scatter in  $Q$  between the two oscillations, which could suggest separate con-  
 835 vective cells in the lava-lake and conduit (Patrick, Orr, Swanson, & Lev, 2016).

### 836 4.3 Timeline of Kīlauea VLP Seismicity

837 Here we present a brief chronological overview of Kīlauea activity and summit VLP  
 838 seismicity from 2008-2018, with particular focus on new observations not discussed in  
 839 previous summaries of Kīlauea activity (Dawson & Chouet, 2014; Anderson et al., 2015;  
 840 Poland & Carbone, 2016; Patrick, Swanson, & Orr, 2019). We break the timeline into  
 841 one or two year long time-segments based on notable changes in VLP seismicity or erup-  
 842 tive activity.

#### 843 4.3.1 January 2008-January 2010: Overlook Crater formation and in- 844 termittent lava-lake

845 The Overlook Crater first began forming inside the Halema‘uma‘u summit crater  
 846 in March 2008, following months of elevated  $\text{SO}_2$  emissions and seismicity (e.g., Patrick  
 847 et al., 2011; Dawson & Chouet, 2014; Patrick, Swanson, & Orr, 2019). Two years of el-

evated seismicity, long-term ground deflation, and occasional explosive events led to the establishment of a persistent lava-lake in early 2010 (Fig. 10). Much of the VLP seismicity during this time was periodic tremor (Fig. S18, S20), though there were times where discrete events were apparent (Fig. S17, S19) (Dawson & Chouet, 2014). Average  $T$  increased and decreased significantly multiple times during this interval, from a maximum of around 25 s in July 2008 to minima of around 13 s in February and August of 2009. While measurements of lava-lake level are limited during this time, the local minima in 2009 correspond with low reported lava-lake levels and the local maxima around July 2008 corresponds with higher reported lava-lake levels (Patrick, Swanson, & Orr, 2019).  $Q$  was highly variable but mostly less than 25. The high variability in  $T$  and  $Q$  over timescales from hours to months during this timespan likely reflects changes in both magma system geometry and magma properties, indicating a highly dynamic shallow magma system.

#### 4.3.2 January 2010-March 2011 Kamoamoia fissure eruption: inflation and lava-lake filling

In early 2010 the lava-lake became persistent and filled from an elevation of 820 m to 950 m by early 2011, accompanied by corresponding long-term ground inflation (Fig. 10). Normal conduit-reservoir events with clear impulsive onsets and decays began occurring during this time, though VLP periodic tremor was also still present (Fig. 12) (Dawson & Chouet, 2014). A more continuous band of conduit-reservoir VLP events began in November 2009 and continued until the March 2011 Kamoamoia fissure eruption. Lava-lake sloshing events with  $T$  around 11 s began to appear alongside some of the Normal conduit-reservoir oscillations (Fig. 10).

The long-term increase in conduit-reservoir  $T$  from  $\sim 20$  s in early 2010 to  $\sim 35$  s by early 2011 is the largest such change observed during the 2008-2018 eruption. Unfeasibly large changes in average magma density and/or density contrast would be required to produce this increase in  $T$  if the shallow magma system geometry were constant, so it is likely that some evolution in geometry occurred over this time. Analysis of ground motion patterns during this time is hindered by limited station availability (Fig. 2). There was a continuous decrease in vertical/horizontal velocity ratios and Mogi source depths from early-mid 2010 (Fig. 16), though these may be partially due to the increasing contribution of tilt with increasing  $T$  (e.g., Maeda et al., 2011). Increases in conduit length of several hundred meters or decreases in conduit radius by around a factor of five could produce the changes  $T$  over this time-segment (Fig. 17). An increase in conduit length by several hundred meters over a 1-yr timescale due to solidification of melt at the roof of an ellipsoidal reservoir is unfeasible (e.g. Karlstrom & Richards, 2011), but could be caused by a migration of the intersection between the conduit and reservoir (e.g., if the conduit connects further down along the sidewalls of an ellipsoidal reservoir or dipping dike). Changes in lava-lake geometry and elevation during this time-segment likely also contribute, but are not considered in detail in existing models (section 4.1).

Our VLP catalog resolves two pronounced  $T$  local maxima in March and June 2010 more clearly than the catalog of Dawson and Chouet (2014); both are about 2 s above the background trend in  $T$  and about a month long. The June maximum corresponded to a pronounced local maximum in ground inflation and lava-lake elevation, but the March maximum is less clearly correlated with ground inflation or lava-lake elevation. For the remainder of this time-segment, conduit-reservoir oscillation  $T$  was well correlated with both ground inflation and lava-lake elevation. There was a gradual increase in  $Q$  starting around August 2010, followed by a rapid drop around February 2011.  $Q$  was correlated with  $T$ , ground inflation, and lava-lake elevation in mid-2010 then became anti-correlated with all three datasets by late 2010. These changes in correlations in early and late 2010 indicate additional changes in the shallow magma system superimposed upon the long-term increase in  $T$  over this time-segment.

900 **4.3.3 March 2011 Kamoamoā fissure eruption-September 2011 Pu‘u ‘Ō‘ō**  
 901 **eruption: multiple East Rift Zone eruption and lava-lake drain-**  
 902 **ing events**

903 After the March 2011 Kamoamoā fissure eruption, there was a gradual increase in  
 904 lava-lake elevation and ground inflation leading up to the August 2011 Pu‘u ‘Ō‘ō erup-  
 905 tion, followed by another short stretch of ground inflation and lava-lake refilling before  
 906 the September 2011 Pu‘u ‘Ō‘ō eruption (Fig. 10). Similar to Dawson and Chouet (2014),  
 907 we do not detect very many VLP events between the March 2011 Kamoamoā and Aug-  
 908 ust 2011 Pu‘u ‘Ō‘ō eruptions, though there were some that exhibited strong glides in  
 909 period. Between the August and September 2011 Pu‘u ‘Ō‘ō eruptions there was a clus-  
 910 ter of low  $Q$  VLP activity with  $T$  around 20 s, and some events that exhibited strong  
 911 glides in period (Fig. S23).

912 It is interesting that there were very few VLP events during most of this time-segment  
 913 even at times when the lava-lake elevation was relatively high, especially since the strongly  
 914 fluctuating lava-lake elevation might be expected to induce abundant rockfalls from the  
 915 crater walls to trigger resonance. The changing lava-lake elevation and good correlation  
 916 between lava-lake elevation and ground inflation during this time indicates that there  
 917 was still an open hydraulic connection between the lava-lake and shallow magma reser-  
 918 voir. However, it is possible that the geometry of the conduit during this time changed  
 919 in a manner that inhibited magma flow on timescales of the conduit-reservoir oscillation  
 920 (e.g., became more constricted or sinuous).

921 **4.3.4 September 2011 Pu‘u ‘Ō‘ō eruption-October 2012 intrusion: lava-**  
 922 **lake filling and reappearance of conduit-reservoir resonance**

923 Between the September 2011 Pu‘u ‘Ō‘ō eruption and May 2012 SSE average lava-  
 924 lake level increased from  $\sim 930$  m to  $\sim 960$  m, although there was only a very slight cor-  
 925 responding ground inflation (Fig. 11). After the May 2012 SSE, which corresponded to  
 926 a temporary 10-day drop in lava-lake elevation, lava-lake elevation and ground inflation  
 927 both decreased until around August, then continually increased until the October 2012  
 928 intrusion. VLP seismicity during this time-segment consisted of Normal and Reverse events,  
 929 VLP periodic tremor, sparse lava-lake sloshing, and gliding-frequency events (Fig. 12,  
 930 S21, S24). Until around the time of the May 2012 SSE conduit reservoir oscillations had  
 931 very low  $Q$ , sometimes below our threshold for robust detections (section 2.3) which con-  
 932 tributes to the apparent sparsity of events (Fig. 11). After the May 2012 SSE average  
 933 conduit-reservoir oscillation  $Q$  continually increased until the October 2012 intrusion.  
 934 Average conduit-reservoir oscillation  $T$  decreased until around August then continually  
 935 increased until the October 2012 intrusion and was well correlated with lava-lake eleva-  
 936 tion (Fig. 15).  $T$  and  $Q$  were positively correlated in late 2012 for the last time in the  
 937 2008-2018 timespan.

938 A steadily widening conduit, perhaps due to thermal erosion and/or increasing mag-  
 939 matic pressure on the conduit walls, could explain the increase in conduit-reservoir  
 940  $Q$  over 2012. A very narrow conduit at the start of this time-segment would also be con-  
 941 sistent with the reduced conduit-reservoir VLP seismicity during the previous time-segment.  
 942 Alternately, the increase in  $Q$  could be caused by a decrease in magma viscosity. This  
 943 would likely not be from a decrease in porosity, since if everything else were constant the  
 944 very gradual ground inflation rate that occurs over this time-segment relative to the lava-  
 945 lake filling rate would imply an increase in magma porosity. Viscosity decreases might  
 946 instead reflect increases in magma temperature, perhaps indicating an influx of hotter  
 947 magma from depth that may have been initiated by the 2012 SSE.

948 **4.3.5 October 2012 intrusion-June 2014 Pu'u 'Ō'ō eruption: stable lava-**  
 949 **lake**

950 Between the October 2012 intrusion and the June 2014 Pu'u 'Ō'ō eruption there  
 951 was a long-term ground inflation trend while average lava-lake level remained constant  
 952 (Fig. 11), though on shorter timescales lava-lake elevation and ground inflation were well  
 953 correlated (Fig. 15). VLP seismicity during this time included both Normal and Reverse  
 954 events, periodic tremor, and lava-lake sloshing (Fig. 12, 13, S22). Until around late 2013  
 955 average conduit-reservoir  $T$  varied from 38-41 s over timescales of months and was gener-  
 956 ally well correlated with lava-lake elevation. After this  $T$  remained relatively constant  
 957 despite continuing fluctuations in lava-lake elevation, and became anti-correlated with  
 958 lava-lake height by April 2014. Average conduit-reservoir  $Q$  decreases from  $\sim 20$  to  $\sim 11$   
 959 by May 2013, followed by a non-monotonic increase to  $\sim 25$  by the June 2014 Pu'u 'Ō'ō  
 960 eruption. Conduit-reservoir  $Q$  was negatively correlated with  $T$  over most of the time-  
 961 segment but exhibited variable correlation with lava-lake elevation and ground inflation.  
 962 Local maxima in conduit-reservoir event density occurred during times of inflation in May  
 963 2013, August 2013, February 2014, and around the May 2014 intrusion (Fig. 13). Conduit-  
 964 reservoir ground motions were constant over this time-segment, indicating a stable reser-  
 965 voir geometry (Fig. 16). Average lava-lake sloshing  $Q$  was highly variable between 6-50  
 966 but increased on average over this time-segment (Fig. 11).

967 The lack of changes in conduit-reservoir ground motions patterns around either the  
 968 October 2012 or May 2014 intrusions likely indicates that these intrusions did not have  
 969 direct enough hydraulic connections to the main shallow reservoir to be involved in the  
 970 oscillations. However, the changes in correlations between  $T$ ,  $Q$ , and lava-lake elevation  
 971 around both intrusions does indicate some change in the shallow magma system. This  
 972 could be related a change in magma properties if some of the shallow magma and/or the  
 973 supply of new melt/volatiles from depth was routed into the intrusions. It is also inter-  
 974 esting that the highest post-2011 VLP event density occurs around the May 2014 intru-  
 975 sion, despite this intrusion having a relatively minor signature in the other datasets.

976 **4.3.6 June 2014 Pu'u 'Ō'ō eruption-May 2016 Pu'u 'Ō'ō eruption: vari-**  
 977 **ation in conduit-reservoir ground motion patterns**

978 There was steady long-term ground inflation during most of this time-segment, with  
 979 more rapid inflation in the months around the May 2015 intrusion (Fig. 11). Lava-lake  
 980 elevation varied between 950-1000 m, except for the months leading up to the May 2015  
 981 intrusion when it increased sharply to 130 m and overflowed out of the overlook crater,  
 982 then sharply dropped following the intrusion. The months after the May 2015 intrusion  
 983 exhibit the only anti-correlation between lava-lake elevation and tilt after 2010 (Fig. 15).  
 984 VLP seismicity during this time-segment included both Normal and Reverse conduit-  
 985 reservoir events, periodic tremor, and lava-lake sloshing (Fig. 13). Local maxima in conduit-  
 986 reservoir event density occurred during the May 2015 intrusion, May 2016 Pu'u 'Ō'ō erup-  
 987 tion, and generally near the onset of long-term inflation periods (for example October  
 988 2014, December 2014, and March 2015). After the June 2014 Pu'u 'Ō'ō eruption there  
 989 was an abrupt change in conduit-reservoir oscillation ground motions apparent as a de-  
 990 crease in vertical/horizontal ratios and in Mogi depths (Fig. 16). Ground motions then  
 991 remained stable until around the October 2015 SSE when they became more variable.  
 992 Conduit-reservoir  $T$  was relatively constant around 39 s except for increasing to 41 s in  
 993 the months leading up to the May 2015 intrusion. Interestingly, the subsequent decrease  
 994 in  $T$  occurred over months despite the rapid drop in lava-lake elevation;  $T$  remained cor-  
 995 related with lava-lake elevation during this time but not with tilt (Fig. 15). There was  
 996 a month-long  $\sim 1$  s local minima in  $T$  corresponding to the October 2015 SSE. Conduit-  
 997 reservoir  $Q$  averaged around 25 until a few months before the May 2015 intrusion, when  
 998 it dropped to around 18 and remained stable for the remainder of the time-segment.  $Q$

999 was either anti-correlated or not correlated with  $T$  during this time-segment and was not  
1000 strongly correlated with lava-lake elevation or ground inflation.

1001 The change in conduit-reservoir event displacement patterns after the June 2014  
1002 Pu'u Ō'ō eruption likely reflects a change in reservoir geometry, and the lack of any cor-  
1003 responding changes in  $T$  or  $Q$  indicates that the conduit geometry probably remained  
1004 constant. Since this change is very abrupt it might reflect the opening/closing of a dike  
1005 or sill, perhaps peripheral structures extending from the main reservoir region. However,  
1006 it is not clear why this would have been related to the ERZ eruption since there were  
1007 apparently no strong changes in summit reservoir pressure. Conduit-reservoir ground mo-  
1008 tions were highly variable around the May 2016 Pu'u Ō'ō eruption, so it is difficult to  
1009 conclude whether this eruption directly corresponded to a change in reservoir geometry  
1010 as the 2014 one did. While there were minimal changes in conduit-reservoir  $T$  and  $Q$ ,  
1011 lava-lake elevation, and ground inflation around the May 2016 Pu'u Ō'ō eruption, an  
1012 abrupt change in  $\text{SO}_2$  emissions indicates that this event did perturb the summit magma  
1013 system.

1014 The anti-correlation between tilt and lava-lake elevation around the May 2015 in-  
1015 trusion is likely because the intruded magma contributed to ground inflation even while  
1016 pressure dropped in the main shallow reservoir. As with the October 2012 and May 2014  
1017 intrusions, the lack of changes in conduit-reservoir ground motion patterns following this  
1018 intrusion indicates that it did not have a direct enough hydraulic connection to the main  
1019 shallow reservoir to be involved in the oscillations. Unlike those earlier intrusions the May  
1020 2015 intrusion does not correspond to clear changes in correlations between  $T$ ,  $Q$ , and  
1021 lava-lake elevation.

1022 Conduit-reservoir events after the October 2015 SSE exhibit increased variability  
1023 in Mogi depths (Fig. 16), but no clear changes in the other metrics for ground displace-  
1024 ment patterns. This could reflect a subtle change in the shallow magma system geom-  
1025 etry or rock properties that made the Mogi inversions more sensitive to noise. Alternately,  
1026 it could indicate that the hydraulic connection to some feature of the shallow magma  
1027 system (e.g., a peripheral dike or sill) is variable over this time. Tectonic stress changes  
1028 from the October 2015 SSE could have conceivably contributed to either scenario.

#### 1029 ***4.3.7 May 2016 Pu'u Ō'ō eruption-May 2018 caldera collapse onset:*** 1030 ***variation in conduit-reservoir ground motion patterns and climac-*** 1031 ***tic eruption precursors***

1032 Long-term averaged lava-lake elevation increased gradually until late 2016 when  
1033 small overflows occurred (Patrick, Swanson, & Orr, 2019), then decreased gradually un-  
1034 til mid-2017. Lava-lake elevation began increasing again more steeply in March 2018 be-  
1035 fore eventually overflowing on April 26, then began draining rapidly on May 2 (e.g., Neal  
1036 et al., 2019) (Fig. 11). There was long term ground inflation over most of this time-segment,  
1037 and lava-lake elevation and ground inflation were mostly correlated on shorter timescales  
1038 except for a few months in mid-2017 (Fig. 15). VLP seismicity during this time included  
1039 Normal and Reverse events, periodic tremor, and lava-lake sloshing (Fig. 12, 13, S12,  
1040 S13, S14). Conduit-reservoir event density was relatively stable over this time-segment,  
1041 while lava-lake sloshing events were numerous until mid-2017 then much sparser after  
1042 this. Conduit-reservoir oscillation  $T$  was stable around 39 s until October 2017 when it  
1043 dropped to 37 s; then increased again in the months leading up to the May 2018 collapse  
1044 eruptions before sharply dropping from 40 s on May 5 to 32 s on May 7 when the last  
1045 definitive conduit-reservoir event in our catalog occurred (Fig. 11). During this time-  
1046 segment  $T$  was alternately correlated and un-correlated or anti-correlated with lava-lake  
1047 elevation and ground inflation (Fig. 15). Conduit-reservoir oscillation  $Q$  remained sta-  
1048 ble around 18 and was anti-correlated with  $T$  until late 2017, when  $Q$  began to vary and  
1049 show a correlation with lava-lake elevation and became uncorrelated with  $T$ . Conduit-

1050 reservoir ground motion patterns remained highly variable over this time-segment, but  
 1051 average Mogi depths decreased until early 2017, after which they remained consistent  
 1052 and with lower misfit (Fig. 16).

1053 That different ground motion metrics show large variability at different times within  
 1054 this time segment indicates that the evolution of reservoir geometry may have been com-  
 1055 plex, but it does seem that some gradual evolution was likely occurring at least until early  
 1056 2017. The numerous changes in correlations around mid-2017 also indicate some change  
 1057 in the shallow magma system. The continual increase in  $T$  in the months leading up to  
 1058 the 2018 collapse eruption onset seems to be similar to the buildup to the October 2012  
 1059 and May 2015 intrusions, which in all three cases seems to track increases in lava-lake  
 1060 elevation and ground inflation indicating a buildup of magma/pressure in the shallow  
 1061 summit magma system. The month-timescale fluctuations in average  $Q$  starting in late  
 1062 2017 indicate some variability in magma properties, but that  $Q$  remains relatively low  
 1063 (mostly  $<20$ ) could indicate that there was not a significant increase in magma temper-  
 1064 ature. This would be consistent with the idea that the increase in pressure could be ex-  
 1065 plained primarily by a blockage along the ERZ rather than by an increase in the flux of  
 1066 new hotter magma from depth (Patrick et al., 2020). Detailed modeling of  $T$ ,  $Q$ , and  
 1067 the other datasets available could yield more insight into what changes in the magmatic  
 1068 system were occurring during this time and what they could have indicated about the  
 1069 upcoming eruptions.

## 1070 5 Conclusions

1071 We have presented a fully automated workflow using wavelet transforms to both  
 1072 detect and categorize VLP seismic signals that arise from magma resonance. These meth-  
 1073 ods can detect multiple distinct spectral peaks and provide robust estimates of quality  
 1074 factors. They do not rely upon any training data and are readily transferable to other  
 1075 volcanoes and to resonant signals in long-period seismic or infrasound data. We expect  
 1076 these methods will be useful for both analyzing historical seismic data and for near-real-  
 1077 time monitoring at various volcanoes.

1078 We then used these methods to generate a catalog of VLP events that occurred be-  
 1079 tween 2008-2018 during a prolonged open vent eruptive episode at Kilauea Volcano, Hawaii  
 1080 USA. This catalog expands upon earlier VLP catalogs by characterizing more types of  
 1081 signals and providing refined estimates of quality factors, revealing new a rich and struc-  
 1082 tured time series of events. We focus particularly on two common classes of events: the  
 1083 ‘conduit-reservoir’ oscillation, which is prevalent over most of this timespan and repre-  
 1084 sents the fundamental eigenmode of the shallow magma plumbing system, and a ‘lava-  
 1085 lake sloshing’ resonance representing surface gravity wave propagation in the summit lava-  
 1086 lake. We document significant changes in period, quality factor, and ground motion pat-  
 1087 terns over timescales ranging from hours to decades for the conduit-reservoir oscillation,  
 1088 including consistent trends around intrusion and eruption events. We also characterize  
 1089 a trend of lava-lake sloshing between 2010 and 2018 that exhibits a relatively consistent  
 1090 increase in period over time but wide variability in quality factors. Both classes of VLP  
 1091 event exhibit variable correlations with each-other and with auxiliary geophysical data  
 1092 such as tilt, lava-lake elevation, and  $\text{SO}_2$  emissions.

1093 The variation in VLP event properties likely indicates changes in magma proper-  
 1094 ties such as density and viscosity in the conduit and lava-lake over timescales ranging  
 1095 from hours to years, as well as both abrupt and gradual changes in magma plumbing sys-  
 1096 tem geometry. This places these resonant oscillations amongst a rich suite of existing data  
 1097 available to understand the evolution of the shallow magma system and processes oc-  
 1098 ccurring in it over the 2008-2018 eruptive episode. We anticipate that future co-inversions  
 1099 of these VLP oscillations and other geophysical data will lead to new insights into the

1100 physical processes responsible for a dynamic and long-lived eruptive episode at Kilauea  
1101 volcano.

## 1102 Appendix A Synthetic Waveform Tests

1103 We construct synthetic seismograms to test the resonant signal detection and clas-  
1104 sification methods described in the methods section. Displacements are calculated from  
1105 an isotropic point source in an elastic half space model (Aki & Richards, 1993), with the  
1106 source located 1 km beneath the Halema‘uma‘u vent. The synthetic source-time func-  
1107 tions consist of combinations of step displacements and exponentially decaying sinusoids  
1108 with impulsive onsets. We apply a sinusoidal taper to the signal onsets to prevent sharp  
1109 discontinuities and create signals with continuous first derivatives (Fig. S26). The sinu-  
1110 soid used as a taper has the same period as the signal, amplitude equal to the initial sig-  
1111 nal amplitude divided by  $\sqrt{2}$ , and is joined at the location where the derivative and po-  
1112 sition of the taper match those of the signal. Where step displacements are also added,  
1113 we taper the step displacement over the same wavelength used to taper oscillation on-  
1114 sets (Fig. S27). We then add white noise from a standard normal distribution, scaled  
1115 to various fractions of the signal amplitude as listed in each test figure. We then calcu-  
1116 late displacements and tilts at each station location using the point source Green’s func-  
1117 tions, and convolve these with the instrument responses (Maeda et al., 2011; Liang, Crozier,  
1118 et al., 2020).

## 1119 Acknowledgments

1120 Additional figures S1-S27 are included in the supplement. The Kilauea VLP seismicity  
1121 catalog is available at (*included as a spreadsheet with this submission, and will also be*  
1122 *uploaded to a data repository consistent with the Enabling FAIR data Project guidelines*  
1123 *prior to publication*). Codes used to make and analyze the VLP catalog are available at  
1124 <https://bitbucket.org/crozierjosh1/vlp-seismicity-catalog-codes/src/master/>, and the au-  
1125 thors will provide updated versions and/or assistance upon request.

1126 Seismic data from 2008-2011 was obtained from the USGS, subsequent seismic data  
1127 is publicly available from IRIS. GPS data is publicly available from UNAVCO. Tilt-meter  
1128 data is available at Johanson (2020). Lava-lake elevation data was obtained from the USGS,  
1129 and is published up to 2018 in Patrick, Swanson, and Orr (2019). SO<sub>2</sub> data from 2007-  
1130 2010 is available at Elias and Sutton (2012). SO<sub>2</sub> emission from 2014-2017 is available  
1131 at Elias et al. (2018). The VLP seismicity catalog extended from the methods of Dawson  
1132 and Chouet (2014) was obtained from the USGS.

1133 We thank Phil Dawson for providing an extended version of the Kilauea VLP cat-  
1134 alog published in 2014, seismic data from before 2012, and discussions of VLP seismic-  
1135 ity categorization. USGS staff including Matt Patrick, Kyle Anderson, and Ingrid Jo-  
1136 hanson provided lava-lake elevation, tilt-meter, and GPS data, as well as discussions about  
1137 Kilauea. Chao Liang and Eric Dunham provided codes and discussions of modeling magma  
1138 resonance. LK acknowledges support from NSF EAR-1624557.

## 1139 References

- 1140 Aki, K., & Richards, P. G. (1993). *Quantitative Seismology* (2nd ed.). University  
1141 Science Books.
- 1142 Alsberg, B. K., Woodward, A. M., & Kell, D. B. (1997, 6). An introduction  
1143 to wavelet transforms for chemometricians: A time- frequency approach.  
1144 *Chemometrics and Intelligent Laboratory Systems*, 37(2), 215–239. doi:  
1145 10.1016/S0169-7439(97)00029-4
- 1146 Anderson, K., Johanson, I., Patrick, M., Gu, M., Segall, P., Poland, M., . . . Mik-  
1147 lius, A. (2019, 12). Magma reservoir failure and the onset of caldera

- 1148 collapse at Kilauea Volcano in 2018. *Science*, *366*(6470), eaaz1822. doi:  
 1149 10.1126/science.aaz1822
- 1150 Anderson, K., & Poland, M. (2016, 8). Bayesian estimation of magma supply,  
 1151 storage, and eruption rates using a multiphysical volcano model: Kilauea Vol-  
 1152 cano, 2000–2012. *Earth and Planetary Science Letters*, *447*, 161–171. doi:  
 1153 10.1016/j.epsl.2016.04.029
- 1154 Anderson, K., Poland, M., Johnson, J., & Miklius, A. (2015). Episodic Defla-  
 1155 tion–Inflation Events at Kilauea Volcano and Implications for the Shallow  
 1156 Magma System. In *Hawaiian volcanoes* (pp. 229–250). American Geophysical  
 1157 Union (AGU). doi: 10.1002/9781118872079.ch11
- 1158 Arciniega-Ceballos, A., Chouet, B., Dawson, P., & Asch, G. (2008, 2). Broad-  
 1159 band seismic measurements of degassing activity associated with lava effusion  
 1160 at Popocatepetl Volcano, Mexico. *Journal of Volcanology and Geothermal*  
 1161 *Research*, *170*(1-2), 12–23. doi: 10.1016/j.jvolgeores.2007.09.007
- 1162 Aster, R. (2003, 11). Very long period oscillations of Mount Erebus Volcano. *Journal*  
 1163 *of Geophysical Research*, *108*(B11). doi: 10.1029/2002jb002101
- 1164 Aster, R., Zandomenighi, D., Mah, S., McNamara, S., Henderson, D., Knox,  
 1165 H., & Jones, K. (2008, 11). Moment tensor inversion of very long pe-  
 1166 riod seismic signals from Strombolian eruptions of Erebus Volcano. *Jour-*  
 1167 *nal of Volcanology and Geothermal Research*, *177*(3), 635–647. doi:  
 1168 10.1016/j.jvolgeores.2008.08.013
- 1169 Baker, S., & Amelung, F. (2012, 12). Top-down inflation and deflation at the sum-  
 1170 mit of Kilauea Volcano, Hawaii observed with InSAR. *Journal of Geophysical*  
 1171 *Research B: Solid Earth*, *117*(12). doi: 10.1029/2011JB009123
- 1172 Battaglia, J. (2003, 12). Location of long-period events below Kilauea Volcano using  
 1173 seismic amplitudes and accurate relative relocation. *Journal of Geophysical Re-*  
 1174 *search*, *108*(B12). doi: 10.1029/2003jb002517
- 1175 Bauer, H. F. (1981). Liquid oscillations with a free surface in wedge-shaped tanks.  
 1176 *Acta Mechanica*, *38*(1-2), 31–54. doi: 10.1007/BF01351461
- 1177 Bell, J. (2014). *Machine Learning*. Indianapolis, IN, USA: John Wiley & Sons, Inc.  
 1178 doi: 10.1002/9781119183464
- 1179 Bergen, K. J., & Beroza, G. C. (2019, 3). Earthquake Fingerprints: Extracting  
 1180 Waveform Features for Similarity-Based Earthquake Detection. *Pure and Ap-*  
 1181 *plied Geophysics*, *176*(3), 1037–1059. doi: 10.1007/s00024-018-1995-6
- 1182 Berger, J., Davis, P., & Ekström, G. (2004, 11). Ambient Earth noise: A survey  
 1183 of the Global Seismographic Network. *Journal of Geophysical Research: Solid*  
 1184 *Earth*, *109*(11), 1–10. doi: 10.1029/2004JB003408
- 1185 Carbone, D., Poland, M., Patrick, M., & Orr, T. (2013). Continuous gravity mea-  
 1186 surements reveal a low-density lava lake at Kilauea Volcano, Hawai‘i. *Earth*  
 1187 *and Planetary Science Letters*, *376*, 178–185. doi: [https://doi.org/10.1016/](https://doi.org/10.1016/j.epsl.2013.06.024)  
 1188 [j.epsl.2013.06.024](https://doi.org/10.1016/j.epsl.2013.06.024)
- 1189 Case, K. M., & Parkinson, W. C. (1957). Damping of surface waves in an incom-  
 1190 pressible liquid. *Journal of Fluid Mechanics*, *2*(2), 172–184. doi: 10.1017/  
 1191 S0022112057000051
- 1192 Cesca, S., Letort, J., Razafindrakoto, H., Heimann, S., Rivalta, E., Isken, M., . . .  
 1193 Dahm, T. (2020, 1). Drainage of a deep magma reservoir near Mayotte in-  
 1194 ferred from seismicity and deformation. *Nature Geoscience*, *13*(1), 87–93. doi:  
 1195 10.1038/s41561-019-0505-5
- 1196 Chevrel, M. O., Harris, A. J., James, M. R., Calabrò, L., Gurioli, L., & Pinkerton,  
 1197 H. (2018, 7). The viscosity of pahoehoe lava: In situ syn-eruptive mea-  
 1198 surements from Kilauea, Hawaii. *Earth and Planetary Science Letters*, *493*,  
 1199 161–171. doi: 10.1016/j.epsl.2018.04.028
- 1200 Chouet, B., & Dawson, P. (2011, 12). Shallow conduit system at Kilauea Volcano,  
 1201 Hawaii, revealed by seismic signals associated with degassing bursts. *JGR*,  
 1202 *116*(12), B12317. doi: 10.1029/2011JB008677

- 1203 Chouet, B., & Dawson, P. (2013, 10). Very long period conduit oscillations induced  
1204 by rockfalls at Kilauea Volcano, Hawaii. *JGR Solid Earth*, *118*(10), 5352–5371.  
1205 doi: 10.1002/jgrb.50376
- 1206 Chouet, B., & Dawson, P. (2016, 8). Origin of the pulse-like signature of shallow  
1207 long-period volcano seismicity. *Journal of Geophysical Research: Solid Earth*,  
1208 *121*(8), 5931–5941. doi: 10.1002/2016JB013152
- 1209 Chouet, B., Dawson, P., James, M., & Lane, S. (2010). Seismic source mechanism of  
1210 degassing bursts at Kilauea Volcano, Hawaii: Results from waveform inversion  
1211 in the 10–50 s band. *JGR*, *115*. doi: 10.1029/2009JB006661
- 1212 Chouet, B., Dawson, P., & Martini, M. (2008, 1). Shallow-conduit dynamics at  
1213 Stromboli Volcano, Italy, imaged from waveform inversions. *Geological Society*  
1214 *Special Publication*, *307*(1), 57–84. doi: 10.1144/SP307.5
- 1215 Chouet, B., & Matoza, R. (2013). A multi-decadal view of seismic methods for  
1216 detecting precursors of magma movement and eruption. *Journal of Volcanol-*  
1217 *ogy and Geothermal Research*, *252*, 108–175. doi: 10.1016/j.jvolgeores.2012.11  
1218 .013
- 1219 Crozier, J., Karlstrom, L., Dufek, J., Anderson, K., Thelen, W., Benage, M.,  
1220 & Liang, C. (2018). Hindcasting May 2018 Kilauea Summit Explo-  
1221 sions with Remote Sensing, Geophysical Monitoring, and Eruption Simu-  
1222 lations. Part 1: Seismic Source Inversions and Self-consistent Initial Con-  
1223 ditions for Plume Models. *AGUFM*, *2018*, V43J-0274. Retrieved from  
1224 <https://ui.adsabs.harvard.edu/abs/2018AGUFM.V43J0274C/abstract>
- 1225 Dawson, P., Benítez, M., Chouet, B., Wilson, D., & Okubo, P. (2010, 9). Monitoring  
1226 very-long-period seismicity at Kilauea Volcano, Hawaii. *Geophysical Research*  
1227 *Letters*, *37*(18), n/a-n/a. doi: 10.1029/2010GL044418
- 1228 Dawson, P., & Chouet, B. (2014, 5). Characterization of very-long-period seismicity  
1229 accompanying summit activity at Kilauea Volcano, Hawai‘i: 2007–2013. *Jour-*  
1230 *nal of Volcanology and Geothermal Research*, *278-279*, 59–85. doi: 10.1016/j  
1231 .jvolgeores.2014.04.010
- 1232 Dawson, P., Chouet, B., Okubo, P., Villaseñor, A., & Benz, H. (1999, 9). Three-  
1233 dimensional velocity structure of the Kilauea Caldera, Hawaii. *GRL*, *26*(18),  
1234 2805–2808. doi: 10.1029/1999GL005379
- 1235 Dawson, P., Chouet, B., & Power, J. (2011, 2). Determining the seismic source  
1236 mechanism and location for an explosive eruption with limited observational  
1237 data: Augustine Volcano, Alaska. *Geophysical Research Letters*, *38*(3), n/a-  
1238 n/a. doi: 10.1029/2010GL045977
- 1239 Edmonds, M., Sides, I., & Maclennan, J. (2015). Insights Into Mixing, Fractiona-  
1240 tion, and Degassing of Primitive Melts at Kilauea Volcano, Hawai‘i. In *Hawai-*  
1241 *ian volcanoes* (pp. 323–349). American Geophysical Union (AGU). doi: 10  
1242 .1002/9781118872079.ch15
- 1243 Edmonds, M., Sides, I., Swanson, D., Werner, C., Martin, R., Mather, T., ... Elias,  
1244 T. (2013, 12). Magma storage, transport and degassing during the 2008-10  
1245 summit eruption at Kilauea Volcano, Hawai‘i. *Geochimica et Cosmochimica*  
1246 *Acta*, *123*, 284–301. doi: 10.1016/j.gca.2013.05.038
- 1247 Elias, T., Kern, C., Horton, K. A., Sutton, A. J., & Garbeil, H. (2018, 12). Mea-  
1248 suring SO<sub>2</sub> Emission Rates at Kilauea Volcano, Hawaii, Using an Array of  
1249 Upward-Looking UV Spectrometers, 2014–2017. *Frontiers in Earth Science*, *6*,  
1250 214. doi: 10.3389/feart.2018.00214
- 1251 Elias, T., & Sutton, A. J. (2012). Sulfur dioxide emission rates from Kilauea Vol-  
1252 cano, Hawai‘i, 2007–2010. *U.S. Geological Survey Open-File Report 2012-1107*,  
1253 25 p. Retrieved from <https://pubs.usgs.gov/of/2012/1107/>
- 1254 Fee, D., & Matoza, R. S. (2013, 1). An overview of volcano infrasound: From  
1255 hawaiian to plinian, local to global. *Journal of Volcanology and Geothermal*  
1256 *Research*, *249*, 123–139. doi: 10.1016/j.jvolgeores.2012.09.002
- 1257 Fowler, A. C., & Robinson, M. (2018, 5). Counter-current convection in a volcanic

- 1258 conduit. *Journal of Volcanology and Geothermal Research*, 356, 141–162. doi:  
 1259 10.1016/j.jvolgeores.2018.03.004
- 1260 Garcés, M., Fee, D., & Matoza, R. (2009, 1). Volcano acoustics. In *Modeling volcanic*  
 1261 *processes: The physics and mathematics of volcanism* (Vol. 9780521895, pp.  
 1262 359–383). Cambridge University Press. doi: 10.1017/CBO9781139021562.016
- 1263 Giordano, D., Russell, J. K., & Dingwell, D. B. (2008, 7). Viscosity of magmatic liq-  
 1264 uids: A model. *Earth and Planetary Science Letters*, 271(1-4), 123–134. doi:  
 1265 10.1016/j.epsl.2008.03.038
- 1266 Gonnermann, H. M., & Manga, M. (2007). The Fluid Mechanics Inside a Volcano.  
 1267 *Annual Review of Fluid Mechanics*, 39(1), 321–356. doi: 10.1146/annurev.fluid  
 1268 .39.050905.110207
- 1269 Goodfellow, I., Bengio, Y. B., & Courville, A. (2016). *Deep Learning*. MIT Press.  
 1270 Retrieved from <http://www.deeplearningbook.org>
- 1271 Haney, M., Chouet, B., Dawson, P., & Power, J. (2013, 6). Source characterization  
 1272 for an explosion during the 2009 eruption of Redoubt Volcano from very-long-  
 1273 period seismic waves. *Journal of Volcanology and Geothermal Research*, 259,  
 1274 77–88. doi: 10.1016/j.jvolgeores.2012.04.018
- 1275 Harris, A. J. (2008, 4). Modeling lava lake heat loss, rheology, and convection. *Geo-*  
 1276 *physical Research Letters*, 35(7), n/a-n/a. doi: 10.1029/2008GL033190
- 1277 Hellweg, M. (2000, 8). Physical models for the source of Lascar’s harmonic tremor.  
 1278 *Journal of Volcanology and Geothermal Research*, 101(1-2), 183–198. doi: 10  
 1279 .1016/S0377-0273(00)00163-3
- 1280 Iacono-Marziano, G., Morizet, Y., Le Trong, E., & Gaillard, F. (2012, 11). New  
 1281 experimental data and semi-empirical parameterization of H<sub>2</sub>O-CO<sub>2</sub> sol-  
 1282 ubility in mafic melts. *Geochimica et Cosmochimica Acta*, 97, 1–23. doi:  
 1283 10.1016/j.gca.2012.08.035
- 1284 Ibrahim, R. A. (2005). *Liquid sloshing dynamics* (Vol. 9780521838). Cambridge Uni-  
 1285 versity Press. doi: 10.1017/CBO9780511536656
- 1286 James, M. R., Lane, S. J., & Corder, S. B. (2008, 1). Modelling the rapid near-  
 1287 surface expansion of gas slugs in low-viscosity magmas. *Geological Society Spe-*  
 1288 *cial Publication*, 307(1), 147–167. doi: 10.1144/SP307.9
- 1289 Jennings, S., Hasterok, D., & Payne, J. (2019). A new compositionally based ther-  
 1290 mal conductivity model for plutonic rocks. *Geophysical Journal International*,  
 1291 219(2), 1377–1394. doi: 10.1093/gji/ggz376
- 1292 Johanson, I. (2020). *Planned USGS Data Release: doi.org/10.5066/P9LBDSDM*.  
 1293 doi: <https://doi.org/10.5066/P9LBDSDM>
- 1294 Johanson, I., Miklius, A., & Poland, M. (2016). Principle component analysis to  
 1295 separate deformation signals from multiple sources during a 2015 intrusive  
 1296 sequence at Kilauea Volcano. *AGUFM, 2016*, G14A-02. Retrieved from  
 1297 <https://ui.adsabs.harvard.edu/abs/2016AGUFM.G14A..02J/abstract>
- 1298 Jolly, A. D., Lokmer, I., Thun, J., Salichon, J., Fry, B., & Chardot, L. (2017, 9).  
 1299 Insights into fluid transport mechanisms at White Island from analysis of  
 1300 coupled very long-period (VLP), long-period (LP) and high-frequency (HF)  
 1301 earthquakes. *Journal of Volcanology and Geothermal Research*, 343, 75–94.  
 1302 doi: 10.1016/j.jvolgeores.2017.06.006
- 1303 Julian, B. R. (1994). Volcanic tremor: nonlinear excitation by fluid flow. *Journal of*  
 1304 *Geophysical Research*, 99(B6). doi: 10.1029/93jb03129
- 1305 Karlstrom, L., & Dunham, E. M. (2016, 6). Excitation and resonance of acoustic-  
 1306 gravity waves in a column of stratified, bubbly magma. *Journal of Fluid Me-*  
 1307 *chanics*, 797, 431–470. doi: 10.1017/jfm.2016.257
- 1308 Karlstrom, L., & Richards, M. (2011, 8). On the evolution of large ultramafic  
 1309 magma chambers and timescales for flood basalt eruptions. *Journal of Geo-*  
 1310 *physical Research: Solid Earth*, 116(8), B08216. doi: 10.1029/2010JB008159
- 1311 Knox, H. A., Chaput, J. A., Aster, R. C., & Kyle, P. R. (2018). Multiyear Shallow  
 1312 Conduit Changes Observed With Lava Lake Eruption Seismograms at Erebus

- 1313 Volcano, Antarctica. *Journal of Geophysical Research: Solid Earth*, 123(4),  
1314 3178–3196. doi: 10.1002/2017JB015045
- 1315 Köcher, S. S., Heydenreich, T., & Glaser, S. J. (2014, 12). Visualization and  
1316 analysis of modulated pulses in magnetic resonance by joint time-frequency  
1317 representations. *Journal of Magnetic Resonance*, 249, 63–71. doi:  
1318 10.1016/j.jmr.2014.10.004
- 1319 Kohler, A., Ohrnberger, M., & Scherbaum, F. (2010, 9). Unsupervised pattern  
1320 recognition in continuous seismic wavefield records using Self-Organizing  
1321 Maps. *Geophysical Journal International*, 182(3), 1619–1630. doi:  
1322 10.1111/j.1365-246X.2010.04709.x
- 1323 Kumagai, H. (2006, 6). Temporal evolution of a magmatic dike system inferred from  
1324 the complex frequencies of very long period seismic signals. *Journal of Geo-  
1325 physical Research: Solid Earth*, 111(6), n/a-n/a. doi: 10.1029/2005JB003881
- 1326 Kumagai, H., & Chouet, B. (2000, 11). Acoustic properties of a crack contain-  
1327 ing magmatic or hydrothermal fluids. *Journal of Geophysical Research: Solid  
1328 Earth*, 105(B11), 25493–25512. doi: 10.1029/2000jb900273
- 1329 Kumagai, H., Miyakawa, K., Negishi, H., Inoue, H., Obara, K., & Suetsugu, D.  
1330 (2003, 3). Magmatic dike resonances inferred from very-long-period seismic  
1331 signals. *Science*, 299(5615), 2058–2061. doi: 10.1126/science.1081195
- 1332 Kumagai, H., Nakano, M., Maeda, T., Yepes, H., Palacios, P., Ruiz, M., ... Ya-  
1333 mashima, T. (2010, 8). Broadband seismic monitoring of active volcanoes  
1334 using deterministic and stochastic approaches. *Journal of Geophysical Re-  
1335 search: Solid Earth*, 115(8). doi: 10.1029/2009JB006889
- 1336 Kumazawa, M., Imanishi, Y., Fukao, Y., Furumoto, M., & Yamamoto, A. (1990, 6).  
1337 A theory of spectral analysis based on the characteristic property of a linear  
1338 dynamic system. *Geophysical Journal International*, 101(3), 613–630. doi:  
1339 10.1111/j.1365-246X.1990.tb05574.x
- 1340 Lapins, S., Roman, D. C., Rougier, J., De Angelis, S., Cashman, K. V., & Kendall,  
1341 J. M. (2020, 1). An examination of the continuous wavelet transform for  
1342 volcano-seismic spectral analysis. *Journal of Volcanology and Geothermal  
1343 Research*, 389, 106728. doi: 10.1016/j.jvolgeores.2019.106728
- 1344 Legrand, D., Kaneshima, S., & Kawakatsu, H. (2000, 8). Moment tensor analysis  
1345 of near-field broadband waveforms observed at Aso volcano, Japan. *Journal of  
1346 Volcanology and Geothermal Research*, 101(1-2), 155–169. doi: 10.1016/S0377-  
1347 -0273(00)00167-0
- 1348 Lesage, P. (2009, 10). Interactive Matlab software for the analysis of seismic volcanic  
1349 signals. *Computers and Geosciences*, 35(10), 2137–2144. doi: 10.1016/j.cageo  
1350 .2009.01.010
- 1351 Lesage, P., Glangeaud, F., & Mars, J. (2002, 5). Applications of autoregressive mod-  
1352 els and time-frequency analysis to the study of volcanic tremor and long-period  
1353 events. *Journal of Volcanology and Geothermal Research*, 114(3-4), 391–417.  
1354 doi: 10.1016/S0377-0273(01)00298-0
- 1355 Liang, C., Crozier, J., Karlstrom, L., & Dunham, E. (2020, 1). Magma Oscilla-  
1356 tions in a Conduit-Reservoir System, Application to Very Long Period (VLP)  
1357 Seismicity at Basaltic Volcanoes: 2. Data Inversion and Interpretation at Ki-  
1358 lauea Volcano. *Journal of Geophysical Research: Solid Earth*, 125(1). doi:  
1359 10.1029/2019JB017456
- 1360 Liang, C., & Dunham, E. (2020, 4). Lava lake sloshing modes during the 2018 Ki-  
1361 lauea Volcano eruption probe magma reservoir storativity. *Earth and Planetary  
1362 Science Letters*, 535, 116110. doi: 10.1016/j.epsl.2020.116110
- 1363 Liang, C., Karlstrom, L., & Dunham, E. (2020, 1). Magma Oscillations in a  
1364 Conduit-Reservoir System, Application to Very Long Period (VLP) Seismic-  
1365 ity at Basaltic Volcanoes: 1. Theory. *Journal of Geophysical Research: Solid  
1366 Earth*, 125(1). doi: 10.1029/2019JB017437
- 1367 Lilly, J. M., & Olhede, S. C. (2009). Higher-order properties of analytic wavelets.

- 1368 *IEEE Transactions on Signal Processing*, 57(1), 146–160. doi: 10.1109/TSP  
 1369 .2008.2007607
- 1370 Lin, G., Shearer, P., Matoza, R., Okubo, P., & Amelung, F. (2014). Three-  
 1371 dimensional seismic velocity structure of Mauna Loa and Kilauea volcanoes  
 1372 in Hawaii from local seismic tomography. *Journal of Geophysical Research:  
 1373 Solid Earth*, 119(5), 4377–4392. doi: 10.1002/2013JB010820
- 1374 Llewellyn, E. W., & Manga, M. (2005, 5). Bubble suspension rheology and impli-  
 1375 cations for conduit flow. *Journal of Volcanology and Geothermal Research*,  
 1376 143(1-3), 205–217. doi: 10.1016/j.jvolgeores.2004.09.018
- 1377 Lokmer, I., Saccorotti, G., Di Lieto, B., & Bean, C. J. (2008, 2). Temporal evolution  
 1378 of long-period seismicity at Etna Volcano, Italy, and its relationships with the  
 1379 2004–2005 eruption. *Earth and Planetary Science Letters*, 266(1-2), 205–220.  
 1380 doi: 10.1016/j.epsl.2007.11.017
- 1381 Lyons, J. J., & Waite, G. P. (2011, 9). Dynamics of explosive volcanism at Fuego  
 1382 volcano imaged with very long period seismicity. *Journal of Geophysical Re-  
 1383 search: Solid Earth*, 116(9). doi: 10.1029/2011JB008521
- 1384 Mader, H., Llewellyn, E., & Mueller, S. (2013, 5). The rheology of two-phase mag-  
 1385 mas: A review and analysis. *Journal of Volcanology and Geothermal Research*,  
 1386 257, 135–158. doi: 10.1016/j.jvolgeores.2013.02.014
- 1387 Maeda, Y., & Takeo, M. (2011, 4). Very-long-period pulses at Asama volcano, cen-  
 1388 tral Japan, inferred from dense seismic observations. *Geophysical Journal In-  
 1389 ternational*, 185(1), 265–282. doi: 10.1111/j.1365-246X.2011.04938.x
- 1390 Maeda, Y., Takeo, M., & Ohminato, T. (2011, 2). A waveform inversion including  
 1391 tilt: Method and simple tests. *Geophysical Journal International*, 184(2), 907–  
 1392 918. doi: 10.1111/j.1365-246X.2010.04892.x
- 1393 Matoza, R., Fee, D., & Garcs, M. (2010, 12). Infrasonic tremor wavefield of  
 1394 the Pu’u ’O’o crater complex and lava tube system, Hawaii, in April 2007.  
 1395 *Journal of Geophysical Research: Solid Earth*, 115(12), B12312. doi:  
 1396 10.1029/2009JB007192
- 1397 Matoza, R., Fee, D., Green, D., & Mialle, P. (2018, 10). Volcano infrasound and the  
 1398 international monitoring system. In *Infrasound monitoring for atmospheric  
 1399 studies: Challenges in middle atmosphere dynamics and societal benefits:  
 1400 Second edition* (pp. 1023–1077). Springer International Publishing. doi:  
 1401 10.1007/978-3-319-75140-5\_{\\_}33
- 1402 McNutt, S., & Roman, D. (2015, 1). Volcanic Seismicity. In *The encyclopedia of vol-  
 1403 canoes* (pp. 1011–1034). Elsevier. doi: 10.1016/b978-0-12-385938-9.00059-6
- 1404 Miklius, A. (2008). *Hawaii GPS Network*. Retrieved from [https://www.unavco](https://www.unavco.org/data/doi/doi-app/does.php?doi=T5RR1WGN)  
 1405 [.org/data/doi/doi-app/does.php?doi=T5RR1WGN](https://www.unavco.org/data/doi/doi-app/does.php?doi=T5RR1WGN) doi: [https://doi.org/10](https://doi.org/10.7283/T5RR1WGN)  
 1406 [.7283/T5RR1WGN](https://doi.org/10.7283/T5RR1WGN)
- 1407 Mogi, K. (1958). Relation between the eruptions of various volcanoes and deforma-  
 1408 tions of the ground surfaces around them. *Bulletin of the Earthquake Research  
 1409 Institute*, 36, 99–134.
- 1410 Montgomery-brown, E., Poland, M., & Miklius, A. (2015, 2). Delicate balance  
 1411 of magmatic-tectonic interaction at Kilauea Volcano, Hawai’i, revealed from  
 1412 slow slip events. In *Geophysical monograph series: Hawaiian volcanoes: From  
 1413 source to surface* (Vol. 208, pp. 269–288). Blackwell Publishing Ltd. doi:  
 1414 10.1002/9781118872079.ch13
- 1415 Mousavi, S. M., Zhu, W., Ellsworth, W., & Beroza, G. (2019, 11). Unsuper-  
 1416 vised Clustering of Seismic Signals Using Deep Convolutional Autoencoders.  
 1417 *IEEE Geoscience and Remote Sensing Letters*, 16(11), 1693–1697. doi:  
 1418 10.1109/LGRS.2019.2909218
- 1419 Nadeau, P., Werner, C., Waite, G., Carn, S., Brewer, I., Elias, T., . . . Kern, C.  
 1420 (2014, 5). Using SO2 camera imagery and seismicity to examine degassing and  
 1421 gas accumulation at Kilauea Volcano, May 2010. *Journal of Volcanology and  
 1422 Geothermal Research*, 300, 70–80. doi: 10.1016/j.jvolgeores.2014.12.005

- 1423 Nakamichi, H., Kumagai, H., Nakano, M., Okubo, M., Kimata, F., Ito, Y., & Obara,  
1424 K. (2009, 11). Source mechanism of a very-long-period event at Mt Ontake,  
1425 central Japan: Response of a hydrothermal system to magma intrusion be-  
1426 neath the summit. *Journal of Volcanology and Geothermal Research*, *187*(3-4),  
1427 167–177. doi: 10.1016/j.jvolgeores.2009.09.006
- 1428 Nakano, M., Kumagai, H., Kumazawa, M., Yamaoka, K., & Chouet, B. (1998, 5).  
1429 The excitation and characteristic frequency of the long-period volcanic event:  
1430 An approach based on an inhomogeneous autoregressive model of a linear  
1431 dynamic system. *Journal of Geophysical Research: Solid Earth*, *103*(B5),  
1432 10031–10046. doi: 10.1029/98jb00387
- 1433 Neal, C., Brantley, S., Antolik, L., Babb, J., Burgess, M., Calles, K., . . . Damby, D.  
1434 (2019, 1). Volcanology: The 2018 rift eruption and summit collapse of Kilauea  
1435 Volcano. *Science*, *363*(6425), 367–374. doi: 10.1126/science.aav7046
- 1436 Orr, T., Poland, M., Patrick, M., Thelen, W., Sutton, A., Elias, T., . . . Wooten,  
1437 K. (2015, 2). Kilauea’s 5–9 march 2011 Kamoamo fissure eruption and  
1438 its relation to 30+ years of activity from Pu’u ‘O’o. In *Geophysical mono-*  
1439 *graph series* (Vol. 208, pp. 393–420). Blackwell Publishing Ltd. doi:  
1440 10.1002/9781118872079.ch18
- 1441 Orr, T., Thelen, W., Patrick, M., Swanson, D., & Wilson, D. (2013). Explosive erup-  
1442 tions triggered by rockfalls at Kilauea volcano, Hawai’i. *Geology*, *41*(2), 207–  
1443 210. doi: 10.1130/G33564.1
- 1444 Owen, S., Segall, P., Lisowski, M., Miklius, A., Denlinger, R., & Sako, M. (2000, 8).  
1445 Rapid deformation of Kilauea Volcano: Global Positioning System measure-  
1446 ments between 1990 and 1996. *Journal of Geophysical Research: Solid Earth*,  
1447 *105*(B8), 18983–18998. doi: 10.1029/2000jb900109
- 1448 Park, I., Jolly, A., Lokmer, I., & Kennedy, B. (2020, 12). Classification of long-  
1449 term very long period (VLP) volcanic earthquakes at Whakaari/White Is-  
1450 land volcano, New Zealand. *Earth, Planets and Space*, *72*(1), 92. doi:  
1451 10.1186/s40623-020-01224-z
- 1452 Patrick, M., Anderson, K., Poland, M., Orr, T., & Swanson, D. (2015, 9). Lava  
1453 lake level as a gauge of magma reservoir pressure and eruptive hazard. *Geol-*  
1454 *ogy*, *43*(9), 831–834. doi: 10.1130/G36896.1
- 1455 Patrick, M., Houghton, B., Anderson, K., Poland, M., Montgomery-Brown, E., Jo-  
1456 hanson, I., . . . Elias, T. (2020). The cascading origin of the 2018 Kilauea  
1457 eruption and implications for future forecasting. *Nature Communications*,  
1458 *11*(1), 5646. doi: 10.1038/s41467-020-19190-1
- 1459 Patrick, M., Orr, T., Anderson, K., & Swanson, D. (2019). Eruptions in sync: Im-  
1460 proved constraints on Kilauea Volcano’s hydraulic connection. *Earth and Plan-*  
1461 *etary Science Letters*, *507*, 50–61. doi: [https://doi.org/10.1016/j.epsl.2018.11](https://doi.org/10.1016/j.epsl.2018.11.030)  
1462 [.030](https://doi.org/10.1016/j.epsl.2018.11.030)
- 1463 Patrick, M., Orr, T., Sutton, A., Lev, E., Thelen, W., & Fee, D. (2016, 1).  
1464 Shallowly driven fluctuations in lava lake outgassing (gas pistoning), Ki-  
1465 lauea Volcano. *Earth and Planetary Science Letters*, *433*, 326–338. doi:  
1466 10.1016/j.epsl.2015.10.052
- 1467 Patrick, M., Orr, T., Swanson, D., & Lev, E. (2016, 12). Shallow and deep controls  
1468 on lava lake surface motion at Kilauea Volcano. *Journal of Volcanology and*  
1469 *Geothermal Research*, *328*, 247–261. doi: 10.1016/j.jvolgeores.2016.11.010
- 1470 Patrick, M., Swanson, D., & Orr, T. (2019, 3). A review of controls on lava lake  
1471 level: insights from Halema’uma’u Crater, Kilauea Volcano. *Bulletin of Vol-*  
1472 *canology*, *81*(3), 1–26. doi: 10.1007/s00445-019-1268-y
- 1473 Patrick, M., Wilson, D., Fee, D., Orr, T., & Swanson, D. (2011). Shallow degassing  
1474 events as a trigger for very-long-period seismicity at Kilauea Volcano, Hawai’i.  
1475 *Bulletin of Volcanology*, *73*(9), 1179–1186. doi: 10.1007/s00445-011-0475-y
- 1476 Perol, T., Gharbi, M., & Denolle, M. (2018, 2). Convolutional neural network for  
1477 earthquake detection and location. *Science Advances*, *4*(2), e1700578. doi: 10

- 1478 .1126/sciadv.1700578  
 1479 Poland, M., & Carbone, D. (2016). Insights into shallow magmatic processes  
 1480 at Kilauea Volcano, Hawaii, from a multiyear continuous gravity time se-  
 1481 ries. *Journal of Geophysical Research: Solid Earth*, *121*(7), 5477–5492. doi:  
 1482 10.1002/2016JB013057
- 1483 Poland, M., Orr, T., Kauahikaua, J., Brantley, S., Babb, J., Patrick, M., . . . Trus-  
 1484 dell, F. (2016, 2). The 2014–2015 Pahoehoe lava flow crisis at Kilauea Volcano,  
 1485 Hawai'i: Disaster avoided and lessons learned. *GSA Today*, *26*(2), 4–10. doi:  
 1486 10.1130/GSATG262A.1
- 1487 Proakis, J. G., & Monolakis, D. G. (1990). *Digital Signal Processing: principles, de-*  
 1488 *vices and applications*. Peter Peregrinus Ltd. doi: 10.1049/pbce042e
- 1489 Ripepe, M., Donne, D. D., Genco, R., Maggio, G., Pistolesi, M., Marchetti, E., . . .  
 1490 Poggi, P. (2015, 5). Volcano seismicity and ground deformation unveil the  
 1491 gravity-driven magma discharge dynamics of a volcanic eruption. *Nature*  
 1492 *Communications*, *6*(1), 1–6. doi: 10.1038/ncomms7998
- 1493 Schaff, D. P. (2008, 6). Semiempirical statistics of correlation-detector perfor-  
 1494 mance. *Bulletin of the Seismological Society of America*, *98*(3), 1495–1507.  
 1495 doi: 10.1785/0120060263
- 1496 Selesnick, I. W., Baraniuk, R. G., & Kingsbury, N. G. (2005). The dual-tree complex  
 1497 wavelet transform. *IEEE Signal Processing Magazine*, *22*(6), 123–151. doi: 10  
 1498 .1109/MSP.2005.1550194
- 1499 Unglert, K., & Jellinek, A. M. (2015, 2). Volcanic tremor and frequency gliding dur-  
 1500 ing dike intrusions at Kilauea—A tale of three eruptions. *Journal of Geophysical*  
 1501 *Research: Solid Earth*, *120*(2), 1142–1158. doi: 10.1002/2014JB011596
- 1502 USGS. (1956). USGS Hawaiian Volcano Observatory (HVO). *Hawaiian Volcano Ob-*  
 1503 *servatory Network*. doi: <https://doi.org/10.7914/SN/HV>
- 1504 USGS. (2020). *USGS: Volcano Hazards Program HVO Kilauea*. Retrieved from  
 1505 [https://volcanoes.usgs.gov/volcanoes/kilauea/multimedia\\_videos](https://volcanoes.usgs.gov/volcanoes/kilauea/multimedia_videos.html)  
 1506 [.html](https://volcanoes.usgs.gov/volcanoes/kilauea/multimedia_videos.html)
- 1507 Wang, K., MacArthur, H., Johanson, I., Montgomery-Brown, E., Poland, M., Can-  
 1508 non, E., . . . Bürgmann, R. (2019, 9). Interseismic Quiescence and Trig-  
 1509 gered Slip of Active Normal Faults of Kilauea Volcano's South Flank During  
 1510 2001–2018. *Journal of Geophysical Research: Solid Earth*, *124*(9), 9780–9794.  
 1511 doi: 10.1029/2019JB017419
- 1512 Wech, A., Thelen, W., & Thomas, A. (2020, 5). Deep long-period earthquakes  
 1513 generated by second boiling beneath Mauna Kea volcano. *Science (New York,*  
 1514 *N.Y.)*, *368*(6492), 775–779. doi: 10.1126/science.aba4798
- 1515 Whitty, R. C., Ilyinskaya, E., Mason, E., Wieser, P. E., Liu, E. J., Schmidt, A., . . .  
 1516 Kern, C. (2020, 2). Spatial and Temporal Variations in SO<sub>2</sub> and PM<sub>2.5</sub> Lev-  
 1517 els Around Kilauea Volcano, Hawai'i During 2007–2018. *Frontiers in Earth*  
 1518 *Science*, *8*, 36. doi: 10.3389/feart.2020.00036
- 1519 Witham, F., & Llewellyn, E. W. (2006, 11). Stability of lava lakes. *Jour-*  
 1520 *nal of Volcanology and Geothermal Research*, *158*(3-4), 321–332. doi:  
 1521 10.1016/j.jvolgeores.2006.07.004
- 1522 Wright, T. L., & Klein, F. W. (2014). Two hundred years of magma transport and  
 1523 storage at Kilauea Volcano, Hawai'i, 1790–2008. *U.S. Geological Survey Profes-*  
 1524 *sional Paper 1806*, 240 p. doi: doi:10.3133/pp1806
- 1525 Yoon, C. E., O'Reilly, O., Bergen, K. J., & Beroza, G. C. (2015, 12). Earthquake de-  
 1526 tection through computationally efficient similarity search. *Science Advances*,  
 1527 *1*(11), e1501057. doi: 10.1126/sciadv.1501057
- 1528 Zadler, B. J., Le Rousseau, J. H., Scales, J. A., & Smith, M. L. (2004, 1). Resonant  
 1529 ultrasound spectroscopy: Theory and application. *Geophysical Journal Inter-*  
 1530 *national*, *156*(1), 154–169. doi: 10.1111/j.1365-246X.2004.02093.x
- 1531 Zuccarello, L., Burton, M., Saccorotti, G., Bean, C., & Patanè, D. (2013, 9). The  
 1532 coupling between very long period seismic events, volcanic tremor, and de-

1533  
1534

gassing rates at Mount Etna volcano. *Journal of Geophysical Research: Solid Earth*, 118(9), 4910–4921. doi: 10.1002/jgrb.50363